arXiv:1501.05954v2 [astro-ph.GA] 27 Apr 2015

SPACE TELESCOPE AND OPTICAL REVERBERATION MAPPING PROJECT.
I. ULTRAVIOLET OBSERVATIONS OF THE SEYFERT 1 GALAXY NGC 5548 WITH
THE COSMIC ORIGINS SPECTROGRAPH ON *HUBBLE SPACE TELESCOPE*

G. De Rosa[1,2,3], B. M. Peterson[1,2], J. Ely[3], G. A. Kriss[3,4], D. M. Crenshaw[5], Keith Horne[6], K. T. Korista[7],
H. Netzer[8], R. W. Pogge[1,2], P. Arévalo[9], A. J. Barth[10], M. C. Bentz[5], W. N. Brandt[11], A. A. Breeveld[12],
B. J. Brewer[13], E. Dalla Bontà[14,15], A. De Lorenzo-Cáceres[6], K. D. Denney[1,2,16], M. Dietrich[17,18], R. Edelson[19],
P. A. Evans[20], M. M. Fausnaugh[1], N. Gehrels[21], J. M. Gelbord[22,23], M. R. Goad[20], C. J. Grier[1,11], D. Grupe[24],
P. B. Hall[25], J. Kaastra[26,27,28], B. C. Kelly[29], J. A. Kennea[11], C. S. Kochanek[1,2], P. Lira[30], S. Mathur[1,2],
I. M. McHardy[31], J. A. Nousek[11], A. Pancoast[29], I. Papadakis[32,33], L. Pei[10], J. S. Schimoia[1,34], M. Siegel[11],
D. Starkey[6], T. Treu[29,35,36], P. Uttley[37], S. Vaughan[21], M. Vestergaard[38,39], C. Villforth[6], H. Yan[40], S. Young[19],
and Y. Zu[1,41]

Draft version April 29, 2015

ABSTRACT

We describe the first results from a six-month long reverberation-mapping experiment in the ultraviolet based on 171 observations of the Seyfert 1 galaxy NGC 5548 with the Cosmic Origins Spectrograph on the *Hubble Space Telescope*. Significant correlated variability is found in the continuum and broad emission lines, with amplitudes ranging from $\sim 30\%$ to a factor of two in the emission lines and a factor of three in the continuum. The variations of all the strong emission lines lag behind those of the continuum, with He II $\lambda1640$ lagging behind the continuum by ~ 2.5 days and Lyα $\lambda1215$, C IV $\lambda1550$, and Si IV $\lambda1400$ lagging by ~ 5–6 days. The relationship between the continuum and emission lines is complex. In particular, during the second half of the campaign, all emission-line lags increased by a factor of 1.3–2 and differences appear in the detailed structure of the continuum and emission-line light curves. Velocity-resolved cross-correlation analysis shows coherent structure in lag versus line-of-sight velocity for the emission lines; the high-velocity wings of C IV respond to continuum variations more rapidly than the line core, probably indicating higher velocity BLR clouds at smaller distances from the central engine. The velocity-dependent response of Lyα, however, is more complex and will require further analysis.

Subject headings: galaxies: active — galaxies: individual (NGC 5548) — galaxies: nuclei — galaxies: Seyfert

[1] Department of Astronomy, The Ohio State University, 140 W 18th Ave, Columbus, OH 43210

[2] Center for Cosmology and AstroParticle Physics, The Ohio State University, 191 West Woodruff Ave, Columbus, OH 43210

[3] Space Telescope Science Institute, 3700 San Martin Drive, Baltimore, MD 21218

[4] Department of Physics and Astronomy, The Johns Hopkins University, Baltimore, MD 21218

[5] Department of Physics and Astronomy, Georgia State University, 25 Park Place, Suite 605, Atlanta, GA 30303

[6] SUPA Physics and Astronomy, University of St. Andrews, Fife, KY16 9SS Scotland, UK

[7] Department of Physics, Western Michigan University, 1120 Everett Tower, Kalamazoo, MI 49008-5252

[8] School of Physics and Astronomy, Raymond and Beverly Sackler Faculty of Exact Sciences, Tel Aviv University, Tel Aviv 69978, Israel

[9] Instituto de Física y Astronomía, Facultad de Ciencias, Universidad de Valparaíso, Gran Bretana N 1111, Playa Ancha, Valparaíso, Chile

[10] Department of Physics and Astronomy, 4129 Frederick Reines Hall, University of California, Irvine, CA 92697

[11] Department of Astronomy and Astrophysics, Eberly College of Science, Penn State University, 525 Davey Laboratory, University Park, PA 16802

[12] Mullard Space Science Laboratory, University College London, Holmbury St. Mary, Dorking, Surrey RH5 6NT, UK

[13] Department of Statistics, The University of Auckland, Private Bag 92019, Auckland 1142, New Zealand

[14] Dipartimento di Fisica e Astronomia "G. Galilei," Università di Padova, Vicolo dell'Osservatorio 3, I-35122 Padova, Italy

[15] INAF-Osservatorio Astronomico di Padova, Vicolo dell'Osservatorio 5 I-35122, Padova, Italy

[17] Department of Physics and Astronomy, Ohio University, Athens, OH 45701

[18] Department of Earth, Environment, and Physics, Worcester State University, 486 Chandler Street, Worcester, MA 01602

[19] Department of Astronomy, University of Maryland, College Park, MD 20742-2421

[20] University of Leicester, Department of Physics and Astronomy, Leicester, LE1 7RH, UK

[21] Astrophysics Science Division, NASA Goddard Space Flight Center, Greenbelt, MD 20771

[22] Spectral Sciences Inc., 4 Fourth Ave., Burlington, MA 01803

[23] Eureka Scientific Inc., 2452 Delmer St. Suite 100, Oakland, CA 94602

[24] Space Science Center, Morehead State University, 235 Martindale Dr., Morehead, KY 40351

[25] Department of Physics and Astronomy, York University, Toronto, ON M3J 1P3, Canada

[26] SRON Netherlands Institute for Space Research, Sorbonnelaan 2, 3584 CA Utrecht, The Netherlands

[27] Department of Physics and Astronomy, Univeristeit Utrecht, P.O. Box 80000, 3508 Utrecht, The Netherlands

[28] Leiden Observatory, Leiden University, PO Box 9513, 2300 RA Leiden, The Netherlands

[29] Department of Physics, University of California, Santa Barbara, CA 93106

[30] Departamento de Astronomia, Universidad de Chile, Camino del Observatorio 1515, Santiago, Chile

[31] University of Southampton, Highfield, Southampton, SO17 1BJ, UK

[32] Department of Physics and Institute of Theoretical and Computational Physics, University of Crete, GR-71003 Heraklion, Greece

[33] IESL, Foundation for Research and Technology, GR-71110 Heraklion, Greece

[34] Instituto de Física, Universidade Federal do Rio do Sul, Campus do Vale, Porto Alegre, Brazil

[35] Department of Physics and Astronomy, University of California, Los Angeles, CA 90095-1547

[37] Astronomical Institute 'Anton Pannekoek,' University of Amsterdam, Postbus 94249, NL-1090 GE Amsterdam, The Netherlands

[38] Dark Cosmology Centre, Niels Bohr Institute, University of Copenhagen, Juliane Maries Vej 30, DK-2100 Copenhagen, Denmark

[39] Steward Observatory, University of Arizona, 933 North Cherry Avenue, Tucson, AZ 85721

[40] Department of Physics and Astronomy, University of Missouri, Columbia, MO 65211

[41] Department of Physics, Carnegie Mellon University, 5000 Forbes Avenue, Pittsburgh, PA 15213

[16] NSF Postdoctoral Research Fellow

[36] Packard Fellow

1. INTRODUCTION

1.1. *The Broad-Line Region*

One of the most prominent characteristics of the ultraviolet (UV), optical, and near-infrared (NIR) spectra of active galactic nuclei (AGNs) is the presence of broad emission lines. While we know that these features arise on scales not much larger than the accretion disk, their physical nature remains one of the major unsolved mysteries in AGN astrophysics. A particularly important feature of the broad emission lines is that they are, by definition, resolved in line-of-sight (LOS) velocity, and their large widths leave little doubt that the primary broadening mechanism is differential Doppler shifts due to the motion of individual gas clouds, filaments, or more-or-less continuous flows around the central black hole.

However, it is not possible to establish the broad-line region (BLR) kinematics simply by inverting the line profiles because this inverse problem is degenerate, with a wide variety of simple velocity models providing satisfactory fits (e.g., Capriotti, Foltz, & Byard 1980). The existing evidence on the BLR kinematics is ambiguous: some of this gas may flow inward, helping to feed the central black hole. Extended, flattened, rotating disk-like structures seem to be important in at least some BLRs, as shown statistically for radio-loud AGNs (Wills & Browne 1986; Vestergaard, Wilkes, & Barthel 2000; Jarvis & McLure 2006), by the pronounced double-peaked profiles observed in some sources (e.g., Eracleous & Halpern 1994, 2003; Strateva et al. 2003; Gezari et al. 2007; Lewis, Eracleous, & Storchi-Bergmann 2010), and from spectropolarimetry (Smith et al. 2004; Young et al. 2007). There is evidence of the importance of the black hole gravity in dominating the motion of the BLR gas (Peterson et al. 2004), although radiation pressure may also play a role (Marconi et al. 2008; Netzer & Marziani 2010).

On the other hand, developments over the last two decades re-open the interesting possibility that much of the emitting BLR gas is due to outflowing winds (e.g., Bottorff et al. 1997; Murray & Chiang 1997; Proga et al. 2000; Everett 2003; Elvis 2004; Young et al. 2007), perhaps connected to the outflows detected in absorption features (e.g., Hamann & Sabra 2004; Krongold et al. 2005, 2007; Kriss et al. 2011; Kaastra et al. 2014; Scott et al. 2014), whose kinematics and energetics are also poorly understood. The unknown dynamics of the BLR gas represents a serious gap in our understanding of AGNs and in the calibrations needed for the study of black-hole/host-galaxy co-evolution up to very high redshifts.

There have been many attempts to model the physics of the BLR. In general, photoionization equilibrium models can reproduce the line intensities, but self-consistent models that provide simultaneous solutions to the line intensities, profiles, and variability are lacking. The locally optimally emitting cloud model (Baldwin et al. 1995; Korista & Goad 2000) and the stratified cloud model (Kaspi & Netzer 1999) explain most observed line intensities and some of the observed time lags between the continuum and emission lines. However, they lack the important kinematic ingredients required to explain the observed line profiles.

1.2. *Reverberation Mapping*

In order to understand the structure and kinematics of the BLR, we must break the degeneracy that comes from the study of the line profiles alone. We can do this by using reverberation mapping (RM) to determine how gas at various LOS velocities responds to continuum variations as a function of light travel-time delay (Blandford & McKee 1982; Peterson 1993, 2014).

Over the last quarter century, the RM technique has become a standard tool for investigating the BLR. In its simplest form, RM is used to determine the mean time delay between continuum and emission-line variations, typically by cross-correlation of the respective light curves. It is assumed that this represents the mean light-travel time across the BLR. By combining this with the emission-line width, which is assumed to reflect the velocity dispersion of gas whose motions are dominated by the mass of the central black hole, the black hole mass can be estimated. RM in this form has been used to measure the black hole masses in over 50 AGNs (for a recent compilation, see Bentz & Katz 2015) to a typical accuracy of ~ 0.3 dex. Important findings that have arisen from these RM studies include the following:

1. In a given AGN, emission lines that are characteristic of higher-ionization gas respond more rapidly to continuum flux variations than those characteristic of lower-ionization gas, indicating ionization stratification within the BLR (Clavel et al. 1991; Reichert et al. 1994).

2. There is an inverse correlation between the time delay, or lag τ, for a particular emission line and the Doppler width ΔV of that emission line. The relationship for a given AGN is consistent with the virial prediction $\Delta V \propto \tau^{-1/2}$ (Peterson & Wandel 1999, 2000; Kollatschny 2003; Peterson et al. 2004; Bentz et al. 2010a). Without this relationship, RM masses would be highly dubious.

3. There is an empirical relationship between the AGN luminosity L and the radius of the BLR R (hereafter the R–L relationship) that is well-established only for the Hβ emission line (Kaspi et al. 2000, 2005; Bentz et al. 2006, 2009, 2013). Limited data on C IV $\lambda1549$ indicates a similar relationship applies to that line as well (Peterson et al. 2005; Vestergaard & Peterson 2006; Kaspi et al. 2007; Park et al. 2013). The existence of R–L relationships for both low-ionization and high-ionization lines has been independently confirmed by gravitational microlensing observations (Guerras et al. 2013).

The R–L relationship is of particular interest as it allows estimation of the central black-hole mass based on a single spectrum from which the line width is measured and the BLR radius is inferred from the AGN luminosity. This neatly bypasses the need for a direct RM measurement of the emission-line time lag. RM is necessarily resource intensive: even to determine the mean time delay for an emission line typically requires some 30–50

well-spaced high-quality spectrophotometric observations or a good measure of luck for fewer observations. The R–L relationship is very important as the RM-based mass determinations anchor empirical scaling relationships (e.g., McLure & Jarvis 2002; Vestergaard 2002; Shields et al. 2003; Grupe & Mathur 2004; Vestergaard 2004; Greene & Ho 2005; Mathur & Grupe 2005; Kollmeier et al. 2006; Vestergaard & Peterson 2006; Salviander et al. 2007; Treu et al. 2007; McGill et al. 2008; Park et al. 2013, 2015; Netzer & Trakhtenbrot 2014) that are used to estimate the masses of quasar black holes in large numbers (e.g., Vestergaard et al. 2008; Vestergaard & Osmer 2009; Shen et al. 2011; De Rosa et al. 2014). Virtually all quasar mass estimates and their astrophysical uses are tied to RM.

Measurement of the mean lag and line width for a given emission line provides important, though limited, information about the BLR and the central mass of the AGN. We are only now beginning to realize the full power of RM through velocity-resolved investigations of the BLR response. The first generation of successful RM programs provided sufficient understanding of AGN variability and BLR response times to design programs that could effectively extract velocity–dependent information that would lead to an understanding of the structure and kinematics of the BLR through recovery of "velocity–delay" maps from RM data (Horne et al. 2004). The relationship between the continuum variations $\Delta C(t)$ and velocity-resolved emission-line variations $\Delta L(V, t)$ is usually described as

$$\Delta L(V, t) = \int_0^\infty \Psi(V, \tau) \Delta C(t - \tau) d\tau, \qquad (1)$$

where $\Psi(V, \tau)$ is the "response function," or velocity–delay map (Horne et al. 2004). As can be seen by inspection, $\Psi(V, \tau)$ is simply the observed emission-line response to a delta-function continuum outburst. The velocity–delay map is simply the BLR geometry and kinematics projected into the two observable quantities of LOS velocity and time delay relative to the continuum. This linearized echo model is justified by the fact that the continuum and emission-line variations are generally quite small (10–20%) on reverberation time scales (see also Cackett & Horne 2006). The technical goal of a reverberation program such as the one described here is to recover the velocity–delay map $\Psi(V, \tau)$ from the data and thus infer the geometry and kinematics of the BLR.

Time-resolved velocity–delay maps have now been obtained for a handful of AGNs (e.g., Bentz et al. 2010b; Brewer et al. 2011; Pancoast et al. 2012; Grier et al. 2013; Pancoast et al. 2014), but only for optical lines (the Balmer lines, He I λ5876, and He II λ4686). In general, these suggest flattened geometries at small to modest inclinations and some combination of virialized motion and infall. An outflow signature has been observed in only one case, NGC 3227 (Denney et al. 2009).

The lack of velocity–delay maps for UV lines, on the other hand, leaves us with a very incomplete understanding of the BLR. It is, in fact, the high-ionization level UV resonance lines (e.g., C IV λ1549, Si IVλ1400, Lyα λ1215) that might be expected to dominate any outflowing component of the BLR. The optical lines, in contrast, generally seem to arise in disk-like structures with infall components (e.g., Pancoast et al. 2014).

RM studies in the UV have been limited. Several observing campaigns were undertaken with the *International Ultraviolet Explorer (IUE)* or *Hubble Space Telescope (HST)* or both on (i) NGC 5548 (Clavel et al. 1991; Korista et al. 1995), (ii) NGC 3783 (Reichert et al. 1994), (iii) Fairall 9 (Clavel, Wamsteker, & Glass 1989; Rodríguez-Pascual et al. 1997), (iv) 3C 390.3 (O'Brien et al. 1998), (v) NGC 7469 (Wanders et al. 1997), (vi) NGC 4151 (Clavel et al. 1990; Ulrich & Horne 1996; Crenshaw et al. 1996), (vii) Akn 564 (Collier et al. 2001), and (viii) NGC 4395 (Peterson et al. 2005). With the exception of Akn 564, which showed essentially no emission-line variability over a comparatively short campaign, all of these programs yielded emission-line lags, but only limited information about the detailed response of the UV emission lines (e.g., Horne, Welsh, & Peterson 1991; Krolik et al. 1991; Wanders et al. 1995; Done & Krolik 1996). The existing velocity-delay map for NGC 4151 shows some incipient structure in C IV λ1549 and He II λ1640 and a general shape that seems to be consistent with a virialized BLR (Ulrich & Horne 1996).

1.3. *The AGN STORM Project*

Given the importance of the UV emission lines in the photoionization equilibrium of the BLR gas and the probable differences between the geometry and kinematics of the high and low-ionization gas in the BLR, we have undertaken a large RM program in the UV using the Cosmic Origins Spectrograph (COS; Green et al. 2012) on *HST* (*HST* Program GO-13330), the AGN Space Telescope and Optical Reverberation Mapping (AGN STORM) Project, in the first half of 2014. The program was designed with certain specific goals in mind:

1. Determine the structure and kinematics of the high-ionization BLR through observations of the variations in the C IV λ1549, Lyα λ1215, N V λ1240, Si IV λ1400, and He II λ1640 emission lines.[42]

2. Carry out simultaneous ground-based observations of (a) the high-ionization optical line He II λ4686 for direct comparison with He II λ1640 and (b) the Balmer lines, particularly Hβ λ4861, to determine the structure and kinematics of the low-ionization BLR. Although the optical spectrum is extremely well-studied (Peterson et al. 2002; Bentz et al. 2007, 2010a; Denney et al. 2010, and references therein), simultaneous observations are necessary, as the dynamical timescale for the BLR in NGC 5548 is only a few years.

3. Compare in detail the continuum variations in the UV (at ~ 1350 Å) with those at other wavelengths (see Edelson et al. 2015, hereafter Paper II) and infer the structure of the continuum-emitting region.

The motivation for the UV/optical continuum comparison is multifold:

---

[42] We note that three of these lines are actually doublets: N V $\lambda\lambda$1239, 1243, Si IV λ1394, 1403, and C IV $\lambda\lambda$1548, 1551. Moreover, the He II feature is blended with O III] $\lambda\lambda$1661, 1665 and Si IV is blended with the quintuplet O IV] $\lambda\lambda$1397.2, 1399.8, 1401.2, 1404.8, 1407.4, where the second, third, and fifth transitions dominate.

1. Delays between continuum variations at longer versus shorter wavelengths have been detected or hinted at in a number of sources (e.g., Wanders et al. 1997; Collier et al. 1998, 2001; Peterson et al. 1998; Sergeev et al. 2005; Cackett, Horne, & Winkler 2007; McHardy et al. 2014; Shappee et al. 2014). Such delays can provide insight into the structure, geometry, and physics of the continuum-emitting region.

2. Velocity–delay maps recovered using the UV continuum as the driving light curve (Equation 1) are expected to be of higher fidelity than those obtained from the optical continuum because the observable UV is closer in wavelength to the ionizing continuum ($\lambda < 912$ Å) that powers the emission lines. The optical continuum is not only a slightly time-delayed version of the UV continuum, but it seems smoothed somewhat as well (Shappee et al. 2014; Peterson et al. 2014), which might make it difficult to recover detailed structure in the velocity–delay maps.

Our *HST* program afforded a valuable opportunity for exploring AGN behavior at high time resolution for an extended period at wavelengths beyond those covered by our *HST* COS spectra. The *HST* program is the anchor of a much broader AGN STORM project to address broader issues through observations across the electromagnetic spectrum. This paper serves as the first in a series.

Of special interest is the possibility of using short-timescale lags between variations in different continuum bands to map the temperature structure of the accretion disk. The *Swift* satellite (Gehrels et al. 2004) is especially suitable for such a study because of its broad wavelength coverage (hard X-ray through *V*-band) and ability to execute high-cadence observations over an extended period of time. In Paper II, we present the results of a four-month program of high-cadence (approximately twice per day) multiwavelength observations with *Swift*. Additional papers in this series will describe high-cadence ground-based photometry from the near UV through the NIR. We will also present results from a program of ground-based spectroscopy that is similar in cadence to the *HST* COS observations, but covers a somewhat longer temporal baseline. Other additional papers will present results on the variable absorption features and on our efforts to decipher the broad emission-line variations and determine the structure and geometry of the BLR.

In Section 2, we describe the observations and data processing, including a discussion of the program design and a complete description of how the standard data reduction pipeline was modified to meet our stringent calibration requirements. We describe our initial data analysis and results in Section 3, and in Section 4, we briefly discuss the first results from our program and place these results in the context of previous monitoring campaigns on NGC 5548. When necessary, we assume a ΛCDM cosmology with $H_0 = 70 \, \mathrm{km^{-1} \, s^{-1} \, Mpc^{-1}}$, $\Omega_M = 0.28$, and $\Omega_\Lambda = 0.72$ (Komatsu et al. 2011).

2. OBSERVATIONS AND DATA REDUCTION

2.1. *Program Design*

RM is a resource-intensive activity that requires obtaining high signal-to-noise ratio (S/N) homogeneous spectra at sufficiently high spectral resolution to resolve the gross kinematics of the BLR. Spectra must be obtained at a high cadence over a temporal baseline that is longer than the typical variability timescale of the AGN. Given the inherent risks of RM programs due to the unpredictability of AGN variability, it is essential that our experimental design assures a successful outcome, yet is as economical with observing time as possible. The first consideration is that each epoch of observation should require no more than one *HST* orbit per "visit" which restricts the integration time per visit to $\sim 45 - 50$ minutes. This consideration limits us to relatively bright nearby Seyfert 1 galaxies. COS is clearly the instrument of choice for such a project, as it is a very sensitive, high spectral resolution spectrometer. Its native resolution ($R > 20000$) is high enough to allow us to trade off resolution and S/N in the data processing phase. In order to schedule the observatory efficiently, a cadence of one visit per day or longer is required.

We therefore want to target an AGN that has a C IV-emitting region several light days in extent, and this requires a source with $\log L_\lambda(1350 \, \text{Å})/(\mathrm{ergs \, s^{-1}}) \gtrsim 43.5$ (e.g., Kaspi et al. 2007). This led us immediately to select as a target the well-studied Seyfert 1 galaxy NGC 5548 ($z = 0.017175$). NGC 5548 is probably the best-studied AGN by RM, with historical optical spectroscopy extending as far back as the early 1970s (Sergeev et al. 2007). Importantly, it has never been known to go into a "dormant state," as observed recently in the case of Mrk 590 (Denney et al. 2014), that would preclude a successful reverberation campaign and, historically, self-absorption in the UV resonance lines has been minimal (Crenshaw & Kraemer 1999), although strong absorption appeared in 2013 (Kaastra et al. 2014).

The remaining adjustable parameter is the duration of the campaign. We investigated this using Monte Carlo simulations similar to those described by Horne et al. (2004). Using recent developments in statistically modeling AGN light curves (Kelly et al. 2009; Kozłowski et al. 2010; MacLeod et al. 2010), we can make very robust models of the expected continuum behavior of NGC 5548. Quasar light curves are well-described by a stochastic process, the damped random walk. The process is described by an amplitude σ and a damping timescale τ_d, which for NGC 5548 in the optical are measured to be $\sigma = 0.89^{+0.30}_{-0.20} \times 10^{-15} \, \mathrm{ergs \, s^{-1} \, cm^{-2} \, \mathring{A}^{-1}}$ and $\tau_d = 77^{+59}_{-34}$ days, respectively (Zu, Kochanek, & Peterson 2011). We used these measured properties of NGC 5548 to simulate the continuum variations; this is a conservative choice as the UV continuum can be expected to show both higher amplitude and shorter time-scale variations, both of which are an advantage. We then convolved the artificial light curves with model velocity–delay maps for several lines to provide an artificial spectrum. As described by Horne et al. (2004), we adopted a BLR model with an extremely challenging velocity–delay map for these simulations, a Keplerian disk with a single two-armed spiral density wave. While this is unlikely to be the actual

AGN BLR geometry, it provides a challenging test: if we can recover such a complex velocity–delay map correctly, then we can certainly hope to recover others of comparable complexity and would have no difficulties with geometries like those that have been recovered for optical lines (e.g., Bentz et al. 2010b; Pancoast et al. 2012; Grier et al. 2013; Pancoast et al. 2014).

We modeled the emissivity and response of each line realistically using a grid of photoionization equilibrium models (Horne et al. 2004). We sampled the artificial spectra to match our proposed observations, including noise. We then modeled the artificial spectra to recover the velocity–delay maps using MEMECHO (Horne 1994; Horne et al. 2004). Simulations based on characteristics of previous RM experiments yield velocity–delay maps with noise levels similar to those obtained from the actual data, demonstrating the verisimilitude of our simulations (see Horne et al. 2004, for examples).

The goal of our simulations was to determine the minimum duration program that would allow us to recover a velocity–delay map with a high probability of success. For COS-like observations (in terms of S/N per visit and spectral resolution), our initial simulations indicated that reliable velocity–delay map recovery for a strong line (e.g., C IV) required between 130 to 200 days. A finer grid of models showed that in 10 of 10 simulations, a high-fidelity velocity–delay map was recovered after 180 days, which was thus adopted as the program goal. A much longer program at this sampling rate would in any case be precluded by the accessibility of the target to *HST*.

Because of the long duration of the proposed program, we also considered the possible impact of losses of data due to instrument or spacecraft safing events. Short safing events occur frequently enough that we needed to assess their impact. Based on the record for *HST* and COS in Cycles 17–20, there might be two spacecraft events that lose 2–3 days each and one COS event that loses 2 days over a stretch of 180 consecutive days. By repeating a subset of our simulations, we found that losses of such small numbers of observations would have no impact on our ability to recover the velocity–delay maps. The simulations also allowed us to assess the impact of early termination of our experiment due to a major failure. If a program was terminated at ~ 100 days, the probability that the data would yield a useful (but not a detailed) velocity–delay map would be $\sim 50\%$. However, a program as short as 75 days would have a very low probability ($\sim 10\%$) of success.

The key to a successful RM campaign is that it must be long enough that favorable continuum variability characteristics become highly probable. That this is essentially guaranteed to happen during a 180-day experiment played a major role in selecting NGC 5548 as our target.

2.2. *COS Observations*

Observations were made in single-orbit *HST* COS visits approximately daily from 2014 February 1 through July 27. Of the 179 scheduled visits, 171 observations were executed successfully and 8 were lost to safing events or target acquisition failures (very close to the expected number of losses).

In each visit, we used the G130M and G160M gratings to observe the UV spectrum over the range 1153–1796 Å in four separate exposures. Exposure times were selected

to provide $S/N \gtrsim 100$ when measured over velocity bins of $\sim 500\,\mathrm{km\,s^{-1}}$. During each visit, we obtained two 200-second exposures with G130M centered at 1291 Å and 1327 Å and two 590-second exposures with G160M centered at 1600 Å and 1623 Å.

The COS far-ultraviolet detector is a windowless, crossed delay-line microchannel plate stack that is subject to long-term charge depletion. To extend the useful lifetime of the detector, we positioned the spectrum so that bright geocoronal airglow lines (e.g., Ly$\alpha\lambda$1215) and AGN emission lines (e.g., redshifted Lyα) would not always fall on the same area of the detector. First, we alternated the target acquisition between the G130M/1291 and the G130M/1327 configurations. The G130M/1327 configuration is then followed by a G130M/1327/FP-POS=3 exposure[43], and by a G130M/1291 exposure alternating among FP-POS=1, 2, and 4. The G130M/1291 configuration is instead followed by a G130M/1291/FP-POS=3 exposure, and by a G130M/1327 exposure alternating among FP-POS=1, 2, and 4. Second, we alternated the FP-POS for the G160M/1623 exposure between FP-POS=1 and FP-POS=2. We could not vary the settings for the G160M/1600 and G160M/1623 further because we needed to ensure the coverage of the entire wavelength range while keeping the detector gap from falling on the redshifted C IV λ1549 emission line.

Finally, we used four additional orbits to improve our understanding of the COS flux calibrations (see Section 2.3). During these additional visits, we observed two of the standard stars (WD 0308–565 and WD 1057+719) employed to obtain sensitivity functions (Massa et al. 2014) at the same detector locations we used for the reverberation program. The observations were taken using all the instrument configurations employed in our primary observing program.

2.3. *Data Reduction*

We used the CalCOS pipeline v2.21 for the bulk of our data processing. The absolute flux calibration of the COS reduction pipeline is reported to be accurate to $\sim 5\%$ and the relative flux calibration is good to better than $\sim 2\%$ (Holland et al. 2014). We are primarily interested in the quality of the relative flux calibration as we are looking for very small-scale variations on short timescales; we need the fluxes to be stable and repeatable across the spectrum. We found, however, that there were local variations in the precision of the fluxes that necessitated improvements.

To produce a final dataset with a flux calibration that is everywhere precise at the 2% level, we refined the existing calibration reference files and applied a post-CalCOS pipeline to further process the data. The main areas of improvement include refinements to the dispersion solution, fixed-pattern noise mitigation, the sensitivity function, and the time dependent sensitivity (TDS) functions, as outlined below. The final data product consists of one combined spectrum per grating per day. Airglow emission lines (O I $\lambda\lambda$1302.2, 1306 and N I $\lambda\lambda$1199.5, 1200.7) were filtered from the data by removing events detected

---

[43] FP-POS values refer to small displacements of the spectrum on the detector in the dispersion direction in order to minimize the effects of fixed-pattern noise.

when *HST* was in daylight. The spectra were further binned by 4 pixels in order to increase the S/N per spectral element of the AGN continuum. This binning still results in two binned pixels per COS resolution element.

2.3.1. *Dispersion solution*

The COS wavelength solution has a quoted uncertainty of $\sim 15\,\mathrm{km\,s^{-1}}$ (Holland et al. 2014). As the STIS uncertainty is $< 5\,\mathrm{km\,s^{-1}}$ (Hernandez et al. 2014), we refined the dispersion solutions for our COS dataset using previous observations of NGC 5548 taken with the STIS E140M/1425 mode in 1998 (PID 7572, PI: Kraemer). To accomplish this, we cross-correlated the line profiles of strong interstellar medium absorption features between each COS observation and the STIS reference spectrum. We used 19 interstellar absorption features, ranging from Si II λ1190 at the short-wavelength end to Al II λ1670 at the long-wavelength end. A linear correction to the initial wavelength solution was then computed across each detector segment and applied directly to the extracted spectra. With this correction, measurements of the root mean square (rms) of the residual offsets decreased from $\sim 15\,\mathrm{km\,s^{-1}}$ to $< 6\,\mathrm{km\,s^{-1}}$.

2.3.2. *Fixed-pattern noise*

The standard reference files used in the `CalCOS` pipeline correct for only the most prominent fixed-pattern noise features such as the quantum-efficiency gridwires, low-order response variations, and large geometric distortion artifacts (Ely et al. 2011). Usually, users combine multiple FP-POS positions to smooth over the remaining features. However, this was not possible for our dataset, since only a single FP-POS setting was used for each central wavelength setting in each orbit (see Section 2.2).

To correct these features to a higher degree we derived one-dimensional pixel-to-pixel flats ("p-flats"). These flats were produced by combining normalized, high signal-to-noise ratio white dwarf spectra in detector space, following the method described by Ely et al. (2011). The white dwarf spectra used were taken as part of the *HST*/CAL program 12806 (PI: Maasa) and used the same detector locations as used for the NGC 5548 datasets.

To test the effects of our p-flat correction, we combined the 171 spectra reduced both with and without the application of the p-flats. The S/N per pixel in 5 Å continuum regions increased from ~ 75 to ~ 80 for the G130M grating, and from ~ 60 to ~ 100 for the G160M grating through the removal of small localized flux calibration errors by the p-flat correction. The improvement for the G130M combined spectrum is less dramatic because (a) we rotated among the four FP-POS settings, and (b) the G130M grating disperses more widely in the cross-dispersion direction, and thus intrinsically averages the fixed-pattern noise over a larger area of the detector.

2.3.3. *Sensitivity functions and TDS*

The COS flux calibration is done in two steps: (a) derivation of static sensitivity functions and (b) characterization of the time evolution of the sensitivity through the TDS correction (Holland et al. 2014). Thanks to the existing calibration program that monitors the TDS variations (PID 13520), we had bi-monthly observations of the standard star WD 0308–565 for 3 out of the 4 central wavelength settings we are using in our program (G130M/1291, G130M/1327 and G160M/1623). Standard star data were obtained in 2014 February, April, June, and August. By analyzing these calibration data, together with the data collected during our additional calibration orbits (Section 2.2), we verified that both the static and time-dependent response functions vary more with instrument configuration than currently modeled by the `CalCOS` pipeline. While `CalCOS` assumes that both the sensitivity function and the TDS correction vary only as a function of wavelength, we were able to improve the relative flux calibrations and reach our required level of precision by (a) obtaining sensitivity functions individually for each configuration (one function per wavelength setting per FP-POS per detector segment), and (b) computing the TDS correction individually for each wavelength setting observed as part of the routine calibration program.

We estimate the quality of the flux calibration by inspection of the fractional residuals f_{res} of the calibrated standard star spectra and their respective `CalSPEC` stellar model (the same models employed by the standard pipeline reference file),

$$f_{\mathrm{res}} = \frac{f_{\mathrm{WD,obs}} - f_{\mathrm{Model}}}{f_{\mathrm{Model}}}, \qquad (2)$$

where both $f_{\mathrm{WD,obs}}$ and f_{Model} are binned over $1\,\text{Å}$ using a boxcar filter in order to increase the S/N per spectral element. While the visual inspection of the residuals as a function of wavelength allows us to identify and correct for local biases, we use the mean value of the distribution of the residuals as an indicator of a global bias in the calibration. The flux calibration uncertainty is an estimate of the limit of the stability of the flux calibration at a given time. However, since the overall instrument sensitivity evolves with time, and our final spectra are obtained from the combination of multiple settings for each grating, we conservatively define the fractional precision error δ_{P} for each grating as the maximum fractional uncertainty computed for any of the wavelength settings.

The new sensitivity functions were derived from spectra of the standard star WD 0308–565 for the G130M settings, and of WD 1057+719 for the G160M settings (PID 12806). While one individual sensitivity function per detector segment characterizes the full grating (data from different settings are averaged together) in `CalCOS`, we built one independent sensitivity function for each wavelength setting and FP-POS used in our program.

By comparing the bi-monthly WD 0308–565 data, we found that residuals with respect to the stellar models were greatly reduced if the TDS corrections were computed individually for each of the wavelength settings (G130M/1291, G130M/1327 and G160M/1623), instead of averaging the data over multiple modes. Additional improvements were obtained by increasing the number of time intervals over which the TDS trends are computed and by redefining the wavelength ranges used in the analysis. Unfortunately, there are insufficient calibration data for the longest wavelengths in the G160M spectra, so we were forced to truncate these spectra at $1750\,\text{Å}$.

In spite of these improvements, the available data did not allow us to conduct any tests on the remaining setting (G160M/1600). This setting is particularly important for our scientific goals since it includes most of the broad C IV emission line (section 1.3). Moreover, since all the calibration data for TDS monitoring purposes are obtained only using FP-POS=3, they did not allow us to test for any residual dependence of the TDS correction on FP-POS configuration. These are the two reasons that motivated us to request further calibration data (see Section 2.2). These data for WD 0308–565 and WD 1057+719 collected in 2014 September allowed us to derive an independent set of sensitivity functions. By comparing the new sensitivity functions with the originals, appropriately corrected for time evolution of the TDS, we were able:

1. To identify the best possible TDS correction attainable for the G160M/1600 setting with the current TDS calibration data. The current `CalCOS` TDS correction for this configuration was obtained from combining both G160M/1577 and G160M/1623 data. Although this correction is not ideal, it minimizes both the global bias and the flux calibration uncertainty when compared to the TDS corrections obtained individually from either the G160M/1577 or the G160M/1623 settings.

2. To verify that the TDS correction does not vary strongly with FP-POS settings. While comparing the residuals with respect to the stellar models shows structure unique to each FP-POS setting, the level of the local biases is such that both the global bias and the flux calibration uncertainty can be considered stable for each wavelength setting (the maximum deviation in the width of the residual distribution is $\sim 0.2\%$).

With the new flux calibration and TDS characterization, our global biases are consistent with zero and the overall fractional precision is $\delta_{\rm P} \sim 1.1\%$ and $\sim 1.4\%$, respectively, for the G130M and G160M settings, compared to $\delta_{\rm P} \sim 1.4\%$ and $\sim 3.5\%$ for the standard pipeline. We intend to make these improvements available to other COS users.

2.3.4. *Sensitivity offsets for the final week of data*

During the final week of the observing campaign, the operating high voltage (HV) for one of the COS detector segments was increased to combat the negative effects of "gain-sag" (Sahnow et al. 2011). While necessary to provide well-calibrated data, this HV change also has the effect of introducing small changes in the detector response. Using WD 0308–565 observations from our calibration orbits taken at the same HV as the rest of the campaign and contemporaneous TDS monitoring observations of the same calibration target (taken at the increased HV), we were able to estimate a HV bias correction for the G130M grating from a direct comparison of the spectra. This bias was measured to be 1% without any detectable dependence on wavelength or cenwave setting. Unfortunately, the same procedure could not be done for the G160M grating as our additional orbits and the TDS observations used different standard stars (WD 0308–565 instead of WD 1057+719). Instead,

the bias estimate for this grating was obtained by analyzing the time evolution of the mean flux in overlapping regions of G130M/1327 at the lower HV setting and G160M/1600 at the higher HV setting. This analysis gave a plausible estimate of a 1% bias. However, with such a limited amount of data at the lower HV and a narrow overlapping wavelength range, the estimate lacks the accuracy of the G130M bias estimate.

3. DATA ANALYSIS

3.1. *Mean and RMS Spectra*

For an initial look at the spectral variations, we define G130M and G160M mean spectra as

$$\overline{F}(\lambda) = \frac{1}{N} \sum_{i=1}^{N} F_i(\lambda) , \qquad (3)$$

where F_i is the ith spectrum of the series of $N = 171$ spectra. Similarly, the rms residual spectrum (hereafter referred to simply as the RMS spectrum) is defined as

$$S(\lambda) = \left\{ \frac{1}{N-1} \sum_{i=1}^{N} \left[F_i(\lambda) - \overline{F}(\lambda) \right]^2 \right\}^{1/2} . \qquad (4)$$

The RMS spectrum is especially useful as it isolates the variable part of the spectrum; constant components disappear, though sometimes small residuals are visible in the case of strong features.

The statistical uncertainty in the mean spectra is

$$\sigma_{\overline{F}}(\lambda) = \frac{1}{N} \left\{ \sum_{i=1}^{N} \sigma_{F_i}^2(\lambda) \right\}^{1/2} , \qquad (5)$$

where σ_{F_i} is the error spectrum of the ith spectrum in the series.

The total uncertainty in the mean spectra consists of this statistical uncertainty and our estimate of the fractional uncertainty in precision as described above, which amounts to $\delta_{\rm P}({\rm G130M}) \approx 1.1\%$ and $\delta_{\rm P}({\rm G160M}) \approx 1.4\%$. To determine the total uncertainty, the statistical uncertainty (Equation 5) and the uncertainty in precision $(\delta_{\rm P}\overline{F}(\lambda))$ are added in quadrature. The mean and RMS spectra for the G130M and G160M settings are shown in Figures 1 and 2, respectively.

The RMS spectrum resulting from Equation (4) combines both the intrinsic variability and the variance due to noise, as discussed by Park et al. (2012) and Barth et al. (2015). In order to isolate the RMS spectrum of the intrinsic variations σ_0, we model the distribution of the residuals of each pixel about the mean. The combined statistical and systematic noise in each pixel of spectrum i is thus $(\sigma_i^2 + (\delta_{\rm P}F_i)^2)^{1/2}$. Assuming that the flux measurement errors and the intrinsic variations arise from independent Gaussian random processes, we find maximum likelihood estimates for the optimal average[44], $\overline{F_\mu}$, and σ_0 by minimizing

$$-2 \ln L \left(\overline{F_\mu}, \sigma_0 \right) = \chi^2 + \sum_{i=1}^{N} \ln \left[\sigma_0^2 + \sigma_i^2 + (\delta_{\rm P}F_i)^2 \right] , \quad (6)$$

[44] The unweighted average $\overline{F}$ in Equation 3 is formally distinct from the optimal average $\overline{F_\mu}$, though practically they are indistinguishable for these data.
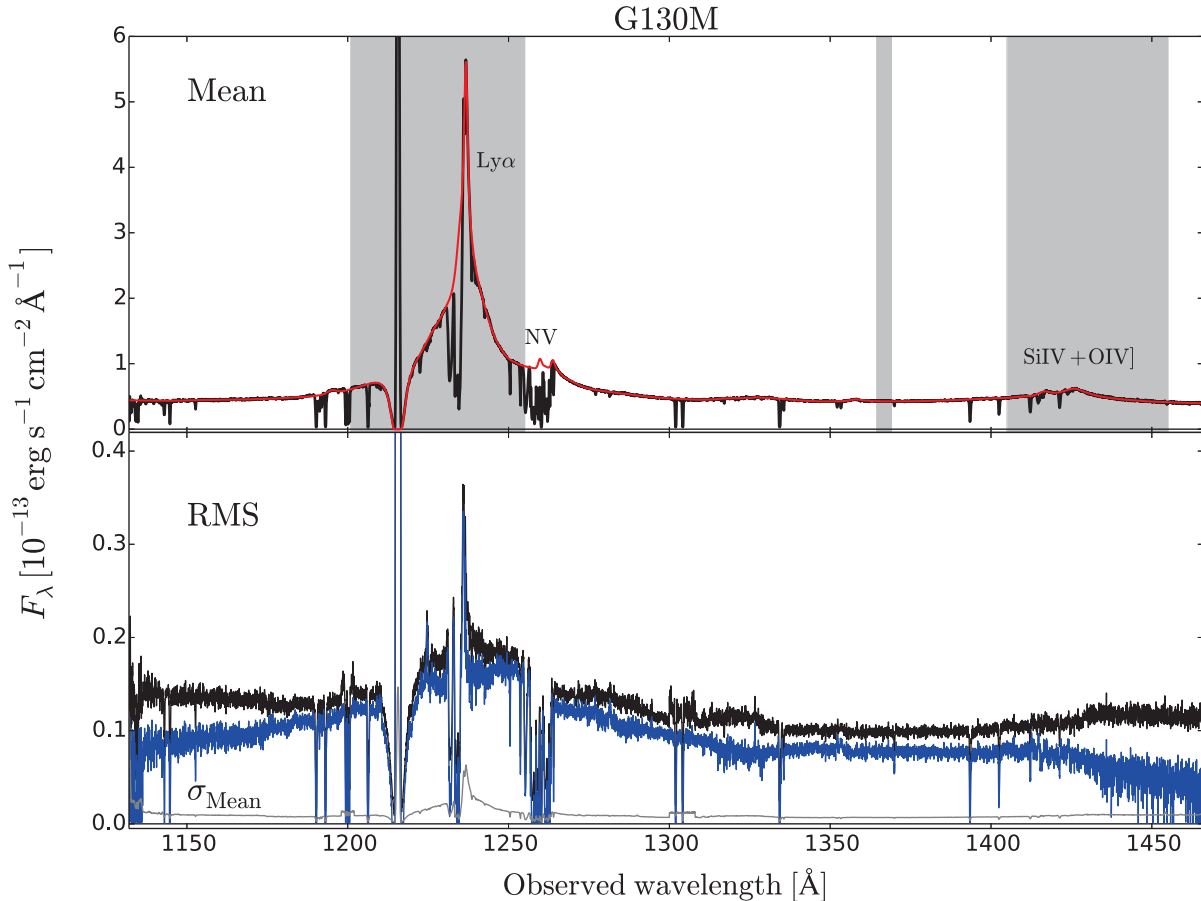
Figure 1. Spectra obtained with the G130M grating. The shaded areas show the integration regions defined in Table 1). Top panel: the mean spectrum, as defined in Equation (3), is shown as a black solid line. The spectral model described in Section 3.5 is shown in red. The deep trough centered at 1215 Å is Galactic Lyα absorption and the strong narrow emission line at the center of this trough is geocoronal Lyα emission. The narrow Galactic absorption lines, although generally saturated, are never black at line center because the thermal broadening of this cold gas is still far below the resolution of COS. Bottom panel: the RMS spectrum, as defined in Equation (4), is shown as a black solid line, while the intrinsic RMS spectrum σ_0 (see Section 3.1) is shown in blue. In grey we show the total error on the mean, which is the statistical error (Equation 5) combined in quadrature with the fractional error in precision, $\delta_P = 1.1\%$ for the G130M spectra. Note the difference in the flux scale between the two panels.

where

$$\chi^2 = \sum_{i=1}^{N} \frac{\left(F_i - \overline{F_\mu}\right)^2}{\sigma_0^2 + \sigma_i^2 + \left(\delta_P F_i\right)^2} \ , \qquad (7)$$

and $\delta_P F_i$ is the precision of the ith spectrum. This estimate of the intrinsic RMS spectrum (σ_0) is also shown in Figures 1 and 2.

3.2. Integrated Light Curves

The next step in our initial analysis is to produce light curves for the continuum and emission lines. At this stage, our goal is to make simple measurements from the reduced spectra, introducing as few assumptions as possible. All flux measurements are performed on spectra in the observed frame. We have not corrected the spectra for Galactic extinction in order to facilitate the cleanest comparison with other measurements to be reported elsewhere in this series of papers (e.g., broad-band photometry).

There are bad pixels throughout the spectrum, and their location and severity change with time, instrument settings, and airglow subtraction (e.g., if a spectrum is taken entirely in orbital bright time, the flux in the air-

glow windows is set to zero and the pixels are flagged as bad pixels). To prevent the introduction of artificial variations in the relative flux estimates, bad pixels are masked throughout the dataset. This means that if a pixel is bad in any of the visits, the pixel is masked out in each of the 171 spectra. We further mask Galactic Lyα absorption and airglow region. Integration ranges (listed in Table 1) were chosen using the mean spectra in Figures 1 and 2 as a guide. Continuum ranges are chosen to be as uncontaminated as possible by absorption lines and broad emission-line wings. In the case of overlapping emission lines (e.g., C IV and He II), the boundary wavelength corresponds to the wavelength at which the fluxes of the two lines are comparable. We do not mask absorption lines at this stage in our analysis. We are unable to cleanly separate N V and Lyα using this simple procedure.

Continuum fluxes are measured as the weighted mean of the flux density in the integration region, with weights equal to the inverse of the variance,

$$F_\lambda = \left(\sum_{i=1}^{N} w_i \ F_i\right)\left(\sum_{i=1}^{N} w_i\right)^{-1} , \qquad (8)$$
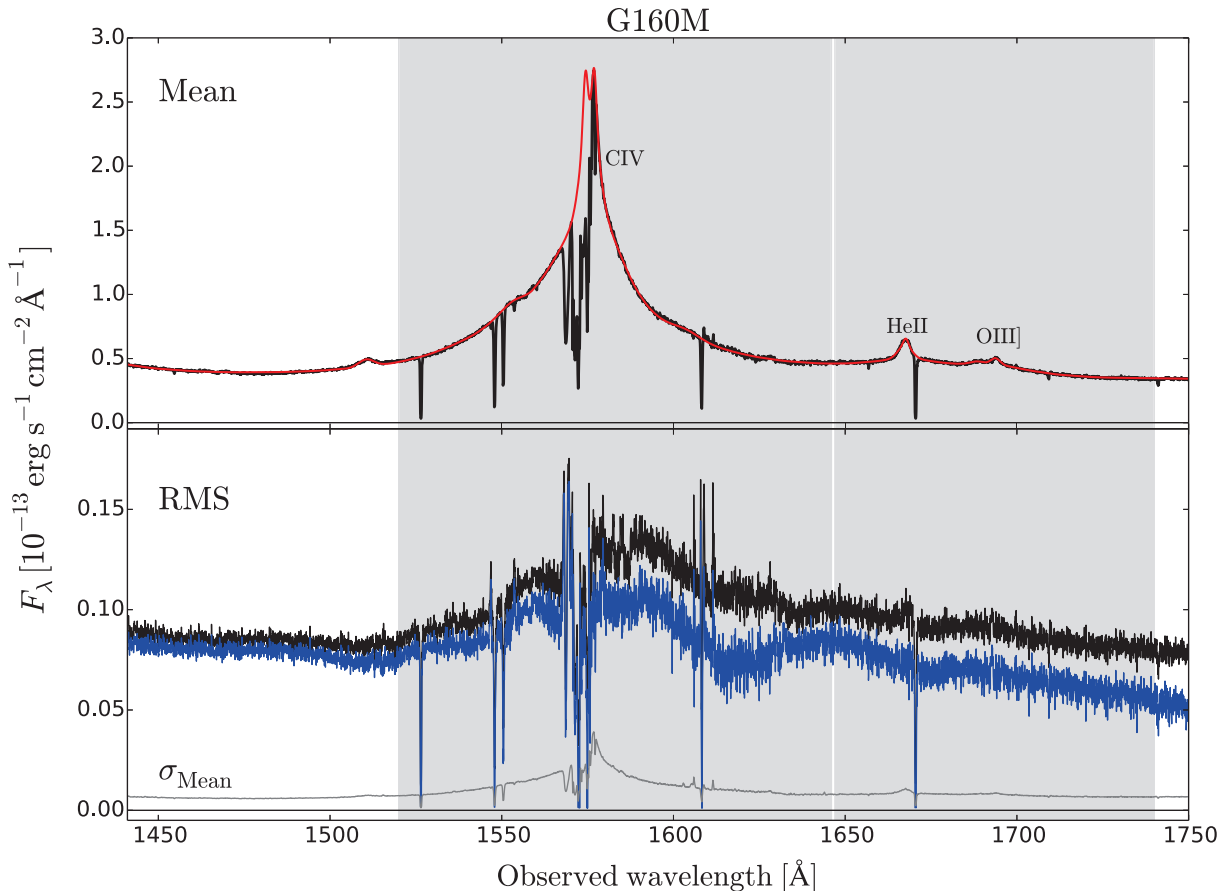
Figure 2. Spectra obtained with the G160M grating. The shaded areas show the integration regions defined in Table 1). Top panel: the mean spectrum, as defined in Equation (3), is shown as a black solid line. The spectral model described in Section 3.5 is shown in red. The narrow Galactic absorption lines, although generally saturated, are never black at line center because the thermal broadening of this cold gas is still far below the resolution of COS. Bottom panel: the RMS spectrum, as defined in Equation (4), is shown as a black solid line, while the intrinsic RMS spectrum σ_0 (see Section 3.1) is shown in blue. In grey we show the total error on the mean, which is the statistical error (Equation 5) combined in quadrature with the fractional error in precision, $\delta_P = 1.4\%$ for the G160M spectra. Note the difference in the flux scale between the two panels.

Table 1
Integration Limits for Light Curves

Emission Component	Integration Limits	Shortward Continuum Region	Longward Continuum Region
F_λ (1367Å)	1364.5–1369.5	–	–
Lyα λ1215	1201.0–1255.0	1155.0–1160.0	1364.5–1369.5
Si IV λ1400[a]	1405.0–1455.0	1364.5–1369.5	1460.0–1463.5
C IV λ1549	1520.0–1646.0	1475.0–1482.0	1743.0–1749.0
He II λ1640[b]	1647.0–1740.0	1475.0–1482.0	1743.0–1749.0

Note. — All regions are in the observed frame (Å).
[a] Integration range also includes O IV] λ1402.
[b] Integration range also includes O III] λ1663.

where $w_i = \sigma_{F_i}^{-2}$ as in Equation (5). Statistical uncertainties computed by `CalCOS` are corrected for low counts following Gehrels (1986). Statistical uncertainties on the mean fluxes are obtained through standard error propagation,

$$\sigma_{F_\lambda} = \left(\sum_{i=1}^{N} w_i \right)^{-1/2}. \qquad (9)$$

In all cases, bad pixels are excluded from the computation.

Emission-line fluxes are measured as the numerical integral of the emission flux above a locally defined continuum defined by the relatively featureless windows given in Table 1. To estimate the local continuum underneath the line we performed a χ^2 linear fit of the continuum flux in the selected regions. The linear local continuum is then subtracted from the emission component, again masking bad pixels. The line flux is numerically integrated over the integration limits given in Table 1 us-

ing Simpson's method. We do not interpolate over bad pixels. We note, however, that the difference between integrating over the bad pixels and computing the integral excluding them is $< 0.1\%$. Statistical errors are computed numerically by creating $N_{\text{sample}} = 5000$ realizations of the line flux and the underlying linear continuum. The flux F_λ is randomly generated from a Gaussian distribution having mean equal to the flux of the spectral element and width σ equal to the statistical error on the flux. For the linear continuum, we generate N_{sample} fits having a mean equal to the best fit values and covariance equal to their covariance matrix. For each realization, a line-flux estimate is then obtained by subtracting the linear continuum and by performing the numerical integration of the residuals. Confidence levels (1σ) are finally obtained from the distribution of the N_{sample} line fluxes. When the error bars are asymmetric, we adopt the larger error as the statistical error associated with the integrated flux.

As noted above, we adopt as the fractional error in precision $\delta_{\text{P}} = 1.1\%$ and $\delta_{\text{P}} = 1.4\%$ for the G130M and G160M settings, respectively. This is added in quadrature to statistical error of the integrated fluxes. The error in the precision dominates throughout the G160M spectra and in the G130M spectra as well, except at wavelengths shortward of $\sim 1180\,\text{Å}$ longward of $\sim 1425\,\text{Å}$, and in the core of the Lyα complex.

The final continuum and emission-line light curves are listed in Table 2 and shown in Figure 3. The light curve statistics are given in Table 3. The average interval between two consecutive observations is $\langle \Delta t \rangle = 1.0$ days with an rms $\sigma(\Delta t) = 0.3$ days. The median interval between observations is $\Delta t_{\text{med}} = 1.0$ days. The largest gaps between consecutive observations are three days (on two occasions) and two days (on six occasions).

3.3. *Time-Series Measurements*

Certain simplifying assumptions underlie the RM technique. Most time-series analyses start with the assumption that the emission-line light curves are simply scaled, time-delayed, and possibly smoothed versions of the continuum light curve. Inspection of the light curves in Figure 3 suggests that this is an entirely reasonable assumption for the first half of the campaign. However, approximately halfway through the campaign, the emission-line response becomes more complicated. Between approximately HJD2456780 and 2456815, the emission-line light curves are either flat (Lyα, He II) or decreasing (C IV) while the continuum is slowly rising. Moreover, the intensity ratio between the last two strong peaks in the continuum light curve at around HJD2456820 and 2456840 seems to be almost inverted in the lines, with the second peak being stronger than the first one (especially in C IV). There is also a small event in the continuum light curve around HJD2456785 that does not appear to have counterparts in the emission-line light curves. The line light curve that seems to best trace the continuum is the He II light curve, which is sensitive to the continuum at energies above 4 Ryd. It is also the only strong line in the COS spectra that is neither a resonance line nor self-absorbed. Moreover, it is the line that arises closest to the continuum source, as we will show below.

Because of the changing character of the emission-line response, for our initial analysis we measure emission-

line lags (a) for the entire data set and (b) for subsets that divide the data into two separate halves of 85 observations each. The first subset, which we will refer to as "T1," runs from HJD2456690 to 2456780 and the second subset, "T2," runs from HJD2456781 to 2456865.

We first measured the emission-line lags relative to the continuum variations by cross-correlation of the light curves. We used the interpolation cross-correlation (ICCF) method as implemented by Peterson et al. (2004). In this method, uncertainties are estimated using a model-independent Monte Carlo method referred to as "flux randomization and random subset selection (FR/RSS)." For each realization, N data points are selected from a light curve with N independent values, without regard to whether or not any particular point has been previously selected. For data points selected n times in a given realization, the flux error associated with that data point is reduced by a factor of $n^{1/2}$. The flux measured at each data point is then altered by adding or subtracting a random Gaussian deviate scaled by the flux uncertainty ascribed to that point. Each realization yields a cross-correlation function that has a maximum linear correlation coefficient r_{max} that occurs at a lag τ_{peak}. We also compute the centroid τ_{cent} of the cross-correlation function using all the points near τ_{peak} with $r(\tau) \geq 0.8\, r_{\text{max}}$. Typically a few thousand realizations are used to construct distribution functions for the ICCF centroid and peak. We adopt the median values of the cross-correlation centroid distribution and the cross-correlation peak distribution as our lag measurements. The uncertainties, which are not necessarily symmetric, correspond to a 68% confidence level. In general, τ_{cent} is found to be a more reliable indicator of the BLR size than τ_{peak}, though we record both. The ICCF measurements of τ_{peak} and τ_{cent} for the four strongest UV emission lines are given in the second and third columns, respectively, in Table 4.

We have also estimated emission-line lags using JAVELIN, which is an improved version of SPEAR (Zu, Kochanek, & Peterson 2011). JAVELIN assumes that the emission-line light curves are shifted and smoothed versions of the continuum light curve (as with the ICCF analysis), where the continuum is modeled as a damped random walk (Kelly et al. 2009; Kozłowski et al. 2010; MacLeod et al. 2010) with uncertainties determined using the Markov Chain Monte Carlo method. We model the full dataset, and each line light curve was run independently with the continuum. The results, given in column (4) of Table 4, are in good agreement with the ICCF analysis, as expected.

In columns (5) and (6) of Table 4, we also give the ICCF centroid values for the T1 and T2 subsets. We also show the ICCFs for the entire sample and the T1 and T2 subsamples in Figure 4. In general, the lags for the T1 subsample have the smallest uncertainties and the ICCFs have the largest peak correlation coefficients r_{max}, as expected. The T2 subset, on the other hand, yields lags with larger uncertainties and ICCFs with lower values of r_{max} (indeed, *much* lower in the case of Si IV and C IV), again as expected from visual inspection of the light curves. The T2 lags are also larger than those from T1, probably only in small part because the continuum is on average brighter (by $\sim 15\%$ on average) during the

Table 2
Continuum and Emission-Line Light Curves

	G130M				G160M	
HJD[a]	F_λ (1367Å)[b]	$F(\mathrm{Ly}\alpha)$[c]	$F(\mathrm{Si\,IV})$[c]	HJD[a]	$F(\mathrm{C\,IV})$[c]	$F(\mathrm{He\,II})$[c]
6690.6120	34.27 ± 0.64	39.66 ± 0.47	4.04 ± 0.26	6690.6479	53.24 ± 0.79	6.92 ± 0.31
6691.5416	35.45 ± 0.65	39.88 ± 0.48	4.47 ± 0.30	6691.5760	53.06 ± 0.79	6.99 ± 0.34
6692.3940	37.71 ± 0.67	39.88 ± 0.48	4.83 ± 0.27	6692.4084	53.30 ± 0.80	6.51 ± 0.35
6693.3237	38.14 ± 0.68	39.22 ± 0.47	4.19 ± 0.28	6693.3380	53.08 ± 0.80	6.64 ± 0.36
6695.2701	40.94 ± 0.71	39.52 ± 0.47	3.92 ± 0.29	6695.3145	53.09 ± 0.81	7.36 ± 0.35
6696.2459	44.25 ± 0.75	39.49 ± 0.48	3.72 ± 0.29	6696.2602	52.76 ± 0.80	7.25 ± 0.36
6697.3080	45.30 ± 0.75	40.16 ± 0.49	4.38 ± 0.30	6697.3223	53.77 ± 0.82	8.00 ± 0.36
6698.3041	48.27 ± 0.79	40.04 ± 0.48	4.14 ± 0.30	6698.3184	55.40 ± 0.83	8.75 ± 0.36
6699.2338	45.80 ± 0.76	41.43 ± 0.51	4.80 ± 0.35	6699.2481	55.65 ± 0.84	8.77 ± 0.37
6700.2299	46.00 ± 0.76	41.13 ± 0.50	4.37 ± 0.30	6700.2442	55.13 ± 0.83	7.73 ± 0.38
6701.3588	47.46 ± 0.78	41.75 ± 0.50	4.52 ± 0.33	6701.3731	54.82 ± 0.83	8.41 ± 0.38
6702.1557	47.74 ± 0.78	41.98 ± 0.51	4.41 ± 0.34	6702.1700	55.64 ± 0.84	8.72 ± 0.39
6703.1518	47.56 ± 0.78	42.33 ± 0.51	4.70 ± 0.32	6703.1661	55.63 ± 0.84	9.27 ± 0.37
6705.3432	45.77 ± 0.76	43.80 ± 0.53	5.57 ± 0.33	6705.3575	57.85 ± 0.86	9.31 ± 0.34

Note. — Full table is given in the published version. Integrated light curves in the observed frame. Flux uncertainties include both statistical and systematic errors.
[a] Midpoint of the observation (HJD − 2450000).
[b] Units of 10^{-15} erg s^{-1} cm^{-2} Å^{-1}.
[c] Units of 10^{-13} erg s^{-1} cm^{-2}.

Table 3
Light Curve Statistics

Emission Component (1)	Mean and RMS Flux (2)	Mean Fractional Error (3)	F_{var}[a] (4)	Maximum Flux (5)	Minimum Flux (6)	R_{max}[b] (7)
F_λ (1367Å)[c]	42.64 ± 8.60	0.017	0.201	64.74	21.87	2.96 ± 0.08
$F(\mathrm{Ly}\alpha)$[d]	41.22 ± 2.71	0.012	0.065	46.84	34.31	1.37 ± 0.02
$F(\mathrm{Si\,IV})$[d]	4.62 ± 0.55	0.065	0.099	6.00	3.23	1.86 ± 0.15
$F(\mathrm{C\,IV})$[d]	53.28 ± 3.91	0.015	0.072	62.97	47.23	1.33 ± 0.03
$F(\mathrm{He\,II})$[d]	7.93 ± 1.13	0.046	0.135	10.62	5.47	1.94 ± 0.12

Note. — Light curves statistics are in the observed frame.
[a] Excess variance, defined as

$$F_{\mathrm{var}} = \frac{\sqrt{\sigma^2 - \delta^2}}{\langle F \rangle} \qquad (10)$$

where σ is the RMS of the observed fluxes (column 2), δ is the mean statistical uncertainty (column 3 times $\langle F \rangle$), and $\langle F \rangle$ is the mean flux in column (2) (Rodríguez-Pascual et al. 1997).
[b] Ratio between maximum and minimum flux.
[c] Units of 10^{-15} erg s^{-1} cm^{-2} Å^{-1}.
[d] Units of 10^{-13} erg s^{-1} cm^{-2}.

Table 4
Emission-Line Lags

Emission Line	τ_{peak}[a]	τ_{cent}[a]	$\tau_{\mathtt{JAVELIN}}$[a]	$\tau_{\mathrm{cent,T1}}$[b]	$\tau_{\mathrm{cent,T2}}$[c]
Lyα	$6.1^{+0.4}_{-0.5}$	$6.19^{+0.29}_{-0.25}$	$5.80^{+0.36}_{-0.39}$	$5.90^{+0.30}_{-0.29}$	$7.73^{+0.76}_{-0.57}$
Si IV	$5.5^{+1.1}_{-1.1}$	$5.44^{+0.70}_{-0.71}$	$5.94^{+0.53}_{-0.55}$	$4.99^{+0.75}_{-0.68}$	$7.22^{+1.33}_{-1.06}$
C IV	$5.2^{+0.7}_{-0.6}$	$5.33^{+0.44}_{-0.48}$	$4.59^{+0.68}_{-0.42}$	$4.61^{+0.36}_{-0.35}$	$9.24^{+1.04}_{-1.04}$
He II	$2.4^{+0.3}_{-0.8}$	$2.50^{+0.34}_{-0.31}$	$2.42^{+0.67}_{-0.06}$	$2.11^{+0.43}_{-0.38}$	$3.87^{+0.71}_{-0.58}$

Note. — Delays measured in light days in the rest frame of NGC 5548.
[a] Complete dataset: 171 visits
[b] T1 dataset: visits 1–85
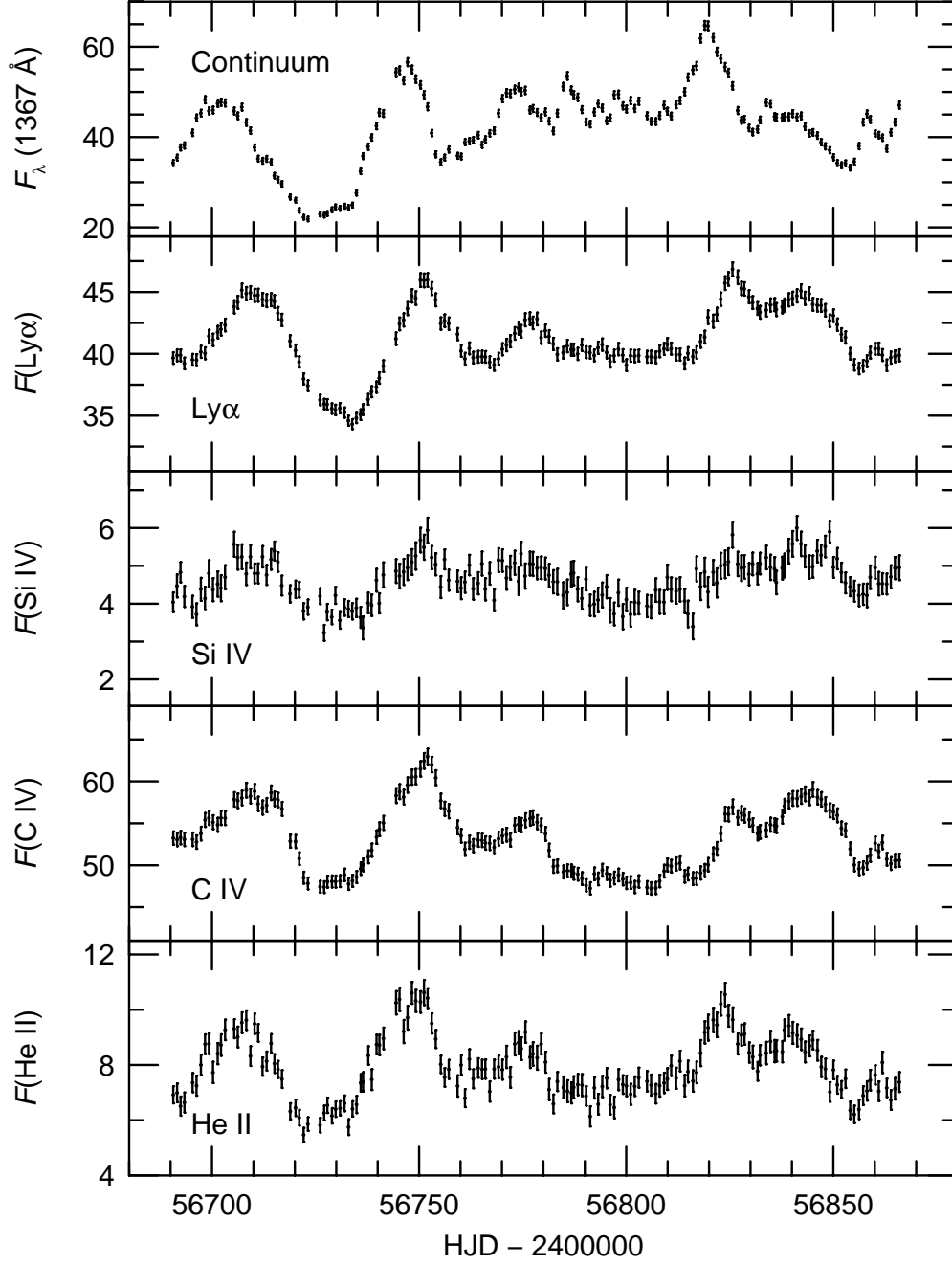[c] T2 dataset: visits 86–171

Figure 3. Integrated light curves. The continuum flux at 1367 Å is in units of 10^{-15} erg s^{-1} cm^{-2} Å^{-1} and the line fluxes are in units of 10^{-13} erg s^{-1} cm^{-2} and are in the observed frame. Flux uncertainties include both statistical and systematic errors.

second half of the campaign so the BLR gas that is most responsive to continuum changes is farther away from the central source.

3.4. *Velocity-Binned Results*

As noted earlier (Section 2.1), this program was designed to recover kinematic information about the BLR by resolving the emission-line response as a function of radial velocity. This will be explored in detail in subsequent papers in this series. Here we carry out a simple preliminary analysis intended to show only whether velocity-dependent information is present in the data. We isolate the Lyα and C IV profiles as described earlier (Section 3.2) but then integrate the fluxes in bins of width 500 km s^{-1}, except in the shortward wing of Lyα ($-10,000$ km s$^{-1} \leq \Delta V \leq -7000$ km s^{-1}) where we use 1000 km s^{-1} bins on account of the low flux in the blue wing of this line.

We show the ICCF centroids for each velocity bin in the C IV emission-line profile in the bottom panel of Figure 5. For the two subsets as well as the entire dataset, we see that there is a clear ordered structure in the kinematics. We cannot infer much from such a simple analysis, of course, because we cannot accurately characterize a complex velocity field with a single number. It is reassuring, however, that the general pattern is similar to what has been seen in other objects and is qualitatively consistent with a virialized region (i.e., the high velocity wings respond first). The middle panel of Figure 5 shows the RMS spectra for the entire dataset and the two subsets.

In the bottom panel of Figure 6, we show the velocity-binned ICCF centroids for the Lyα emission line. Again, a clear pattern emerges, as the lags in each velocity bin are highly correlated with those of adjacent bins. However, the pattern that emerges is unlike what is seen in C IV; the largest lags are at intermediate velocities and the lags decrease toward line center. However, given the severe blending and strong absorption, detailed modeling will be required before any meaningful conclusions can be drawn.

3.5. *Modeling the mean spectrum*

The mean spectra shown in Figures 1 and 2 can be compared with earlier UV spectra of NGC 5548 obtained with *HST* (e.g., Korista et al. 1995; Kaastra et al. 2014). The earliest high-quality UV spectra of NGC 5548 showed only weak absorption in the resonance lines (Lyα, N V, Si IV, and C IV), a factor that contributed to our selection of NGC 5548 as a target for this investigation. The 2013 spectra (Kaastra et al. 2014), however, revealed not only several strong narrow absorption features in the resonance lines, but also evidence for a relatively large "obscurer" that strongly absorbs the emission in the blue wings of the resonance lines. This feature is still present in our spectra obtained a year later, but is weaker than it was in 2013. The presence of this absorption, combined with the blending of various emission features (Lyα and N V, Si IV and O IV], C IV and He II), complicates analysis of these spectra. To characterize the emission-line structure of NGC 5548 and guide our selection of continuum windows for our emission-line flux measurements, we fit a heuristic model to the lines

and continuum in the mean spectra. Our model for NGC 5548 is similar to that adopted by Kaastra et al. (2014), and it includes the broad absorption features associated with all permitted transitions in the spectrum. Our adopted continuum is a reddened power law of the form $F_\lambda(\lambda) = F_\lambda(1000\,\text{Å})(\lambda/1000\,\text{Å})^{-\alpha}$. We correct for $E(B-V) = 0.017$ mag of Galactic extinction (Schlegel, Finkbeiner, & Davis 1998; Schlafly & Finkbeiner 2011) using the prescription of Cardelli, Clayton, & Mathis (1989) and $R_V = 3.1$. We do not apply any correction for possible internal extinction in NGC 5548. Longward of 1550 Å, we also include blended Fe II emission as modeled by Wills, Netzer, & Wills (1985), broadened with a Gaussian with full-width at half-maximum FWHM = 4000 km s^{-1}. We model the emission lines with multiple Gaussian components. These are not an orthogonal set, and the decomposition is not rigorously unique, but they characterize each line profile well.

For the brightest lines, we start with a narrow component, typically with FWHM ≈ 300 km s^{-1}. This component is essentially identical to the narrow component used by Crenshaw et al. (2009) for fitting the 2004 STIS spectrum of NGC 5548. Since this narrow component is difficult to deblend from the broader components of each line, and since Crenshaw et al. (2009) saw little variation in narrow-line intensity over time, we fix the flux and widths of the narrow components of Lyα, N V, C IV, and He II to the values we used to fit the 2004 STIS spectrum. The Si IV lines do not have a detectable narrow-line component. We note that while Peterson et al. (2013) detected changes in the strength of the narrow [O III] $\lambda\lambda$4959, 5007 lines over timescales of years, the variations over the last decade have been only at the few percent level. Similar variations in the narrow components of the UV lines would not be easily detected here because the narrow components are all so weak.

Next we add an intermediate-width component with FWHM ≈ 800 km s^{-1} without ascribing physical meaning to it, using the STIS 2004 spectrum as a model. An intermediate-width component is included in Lyα, N V, Si IV, C IV, and He II, as well as in the fainter lines C III* λ1176, Si II λ1260, Si II+O I λ1304, C II λ1335, N IV] λ1486, O III] λ1663, and N III] λ1750. For the weaker lines, this is often the only component detected, so its flux, width, and position are all allowed to vary. For the stronger lines, as for the NLR components, we again keep the fluxes and widths of the intermediate-width components fixed at the values found for the STIS 2004 spectrum since Crenshaw et al. (2009) found that these components vary only slightly in flux over several years. For the stronger lines, we next include broader components with FWHM ≈ 3000, 8000, and 15,000 km s^{-1}, respectively. For the doublets of N V, Si IV, and C IV, we assume the line-emitting gas is optically thick and fix the flux ratio of each pair to 1:1, although for the 15,000 km s^{-1} component, only a single Gaussian is used. Finally, as can be seen in the RMS spectrum in Figure 2, there are two weak bumps that appear on the red and blue wings of the C IV emission-line profile at ~ 1554 Å and ~ 1604 Å in the observed frame. These bumps are also present in the mean spectrum; we include a single Gaussian component to account for each of these bumps.
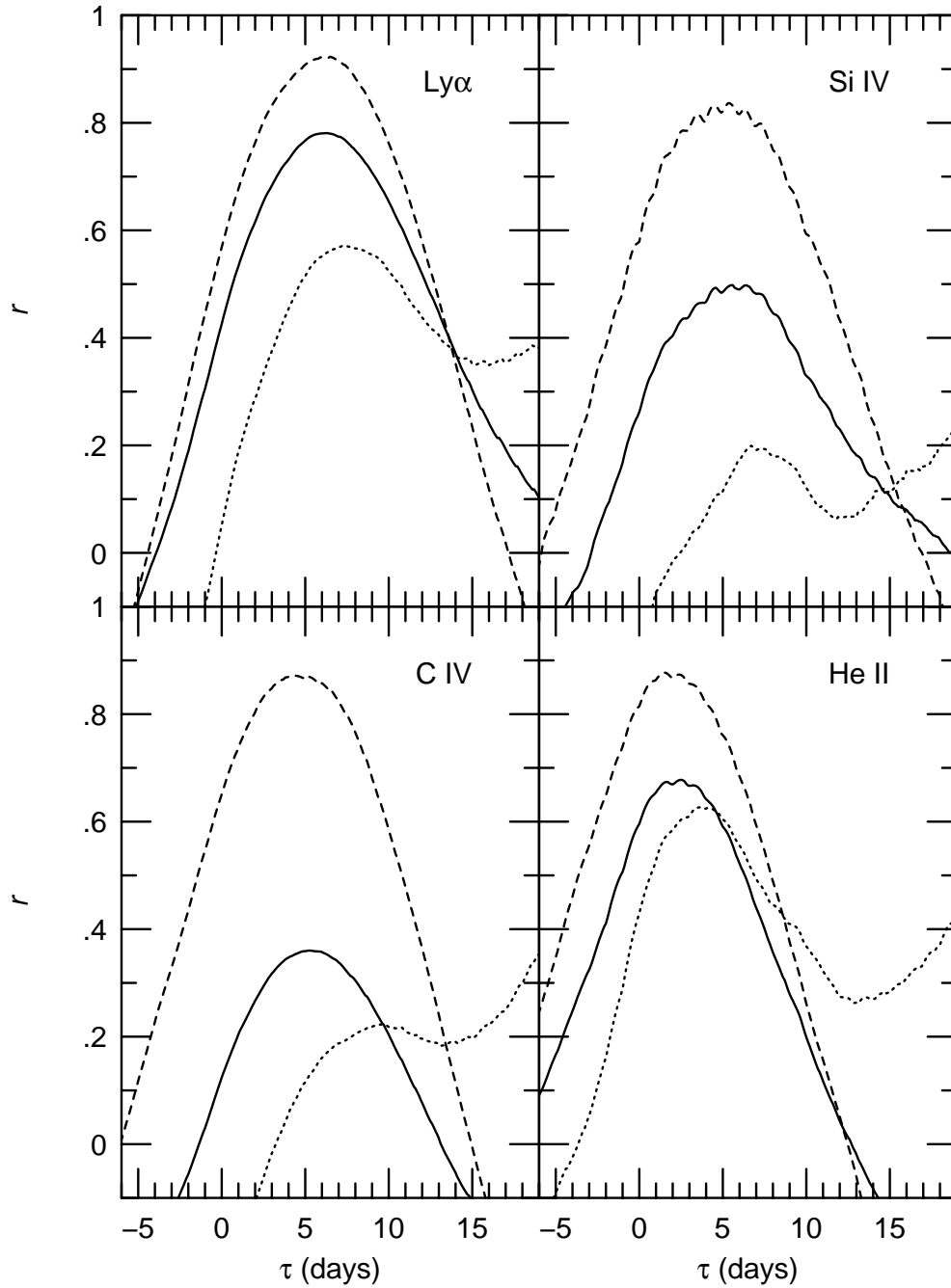
Figure 4. Interpolated cross-correlation functions (ICCFs) computed by cross-correlating each emission-line light curve with the 1367 Å continuum light curve. The solid line is the ICCF for the entire data set. The dashed line is for the T1 subsample (the first 85 visits) and the dotted line is for the T2 subsample (the last 85 visits).
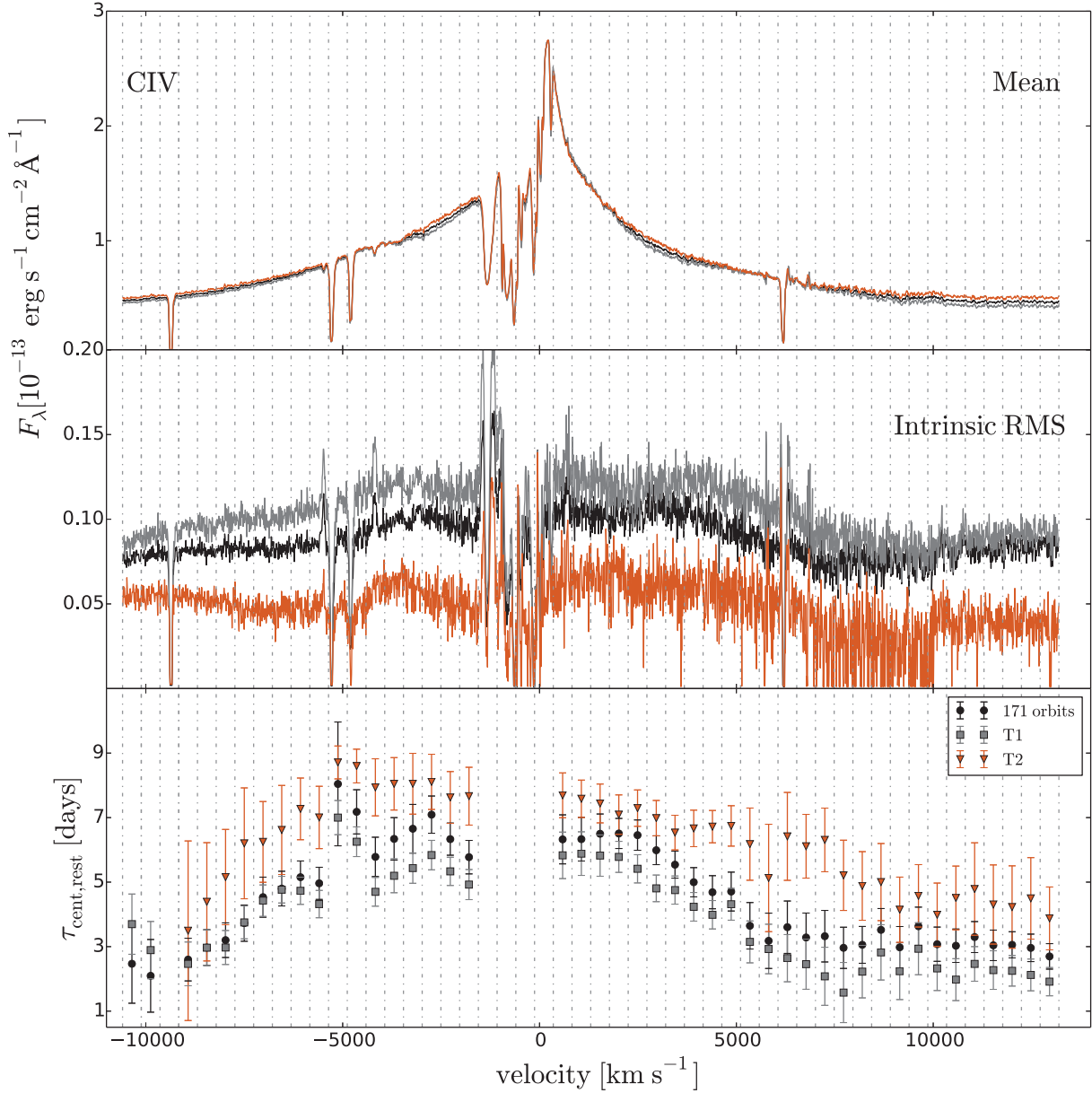
Figure 5. Velocity-binned results for the C IV λ1549 emission line. The top and middle panels show the mean and intrinsic RMS (σ_0) spectra, respectively. The bottom panel shows the centroid of the cross-correlation function for each individual velocity bin, corrected to the rest frame of NGC 5548. Velocity bins with no lag measurement contain too little total flux to reliably characterize the variations. In each case, the black line represents the entire dataset, and the T1 (first 85 visits) and T2 (last 85 visits) subsets are shown in gray and orange, respectively. Note that the shortest lags are found for the highest-velocity gas.
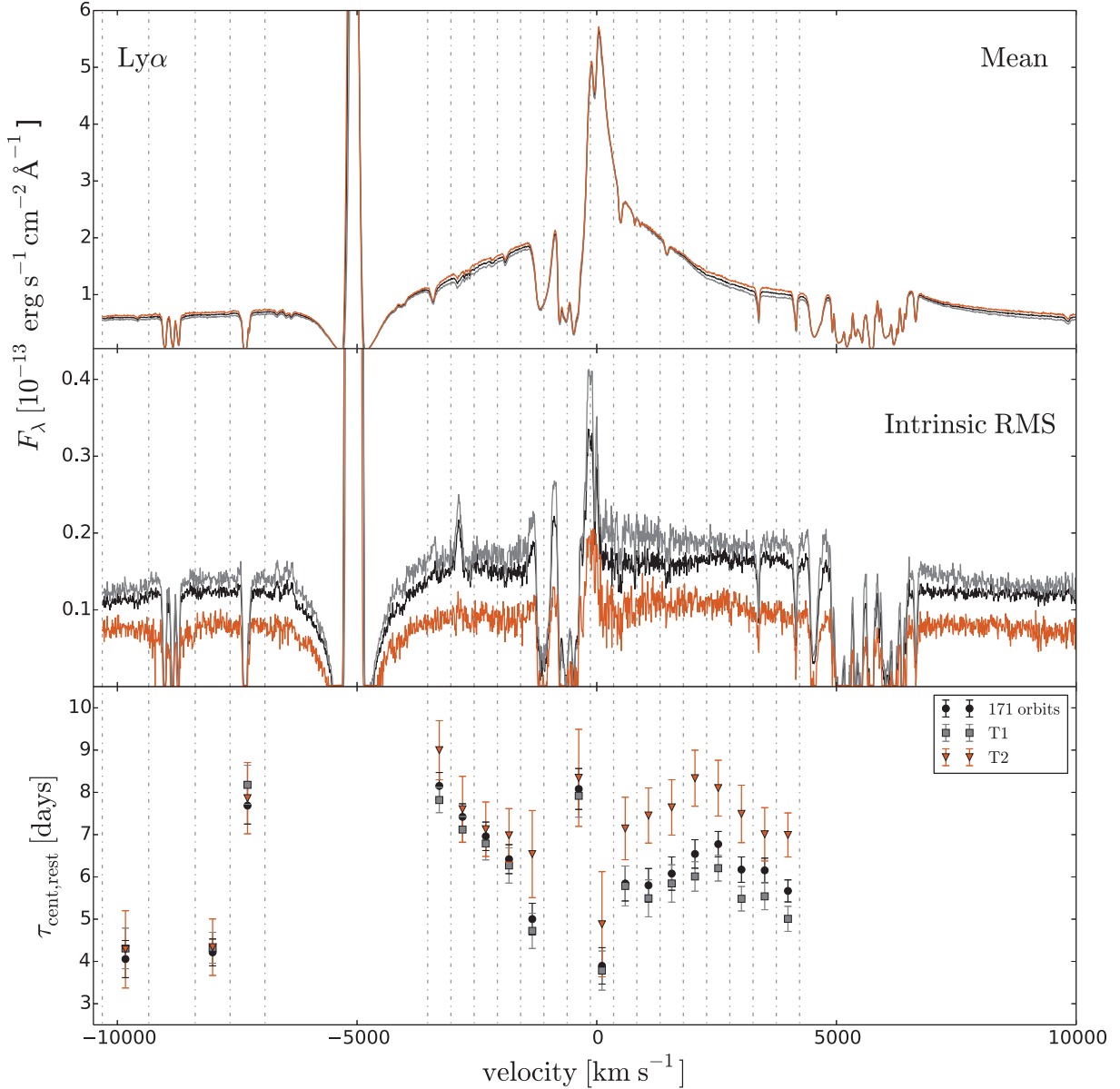
Figure 6. Velocity-binned results for the Lyα $\lambda1215$ emission line. The top and middle panels show the mean and intrinsic RMS (σ_0) spectra, respectively. The bottom panel shows the centroid of the cross-correlation function for each individual velocity bin, corrected to the rest frame of NGC 5548. Velocity bins with no lag measurement contain too little total flux to reliably characterize the variations. In each case, the black line represents the entire dataset, and the T1 (first 85 visits) and T2 (last 85 visits) subsets are shown in gray and orange, respectively. The large gap at around $-5000\,\mathrm{km\,s^{-1}}$ avoids the region of the spectrum affected by geocoronal emission and Galactic absorption.

As described by Kaastra et al. (2014), we use an asymmetric Gaussian with negative flux to model the broad absorption troughs. The asymmetry in these Gaussian profiles is introduced by specifying a larger dispersion on the blue side of line center than on the red side. The asymmetry is fitted as a free parameter, and the resultant absorption line has a roughly rounded triangular shape with a blue wing extending from the deepest point in the absorption profile (for an illustration, see Kaastra et al. 2014). During the first part of our reverberation campaign, when these absorption features were strongest, an additional depression appeared on the high-velocity blue tail of the main absorption trough. We use a single, symmetric Gaussian to model the shape of this additional shallow depression. For absorption by N V, Si IV, and C IV, since the individual doublet profiles are unresolved, we assume the lines are optically thick, so each line in the doublet has the same strength and profile.

As a final component, we include absorption by damped Galactic Lyα with a column density of $N(\mathrm{H\,I}) = 1.45 \times 10^{20}\,\mathrm{cm^{-2}}$ (Wakker, Lockman, & Brown 2011). The full spectral model for NGC 5548, excluding the narrow absorption, is shown in the upper panels of Figure 1 and Figure 2, superposed on the observed mean spectra.[45] In future papers, we will apply this model to

[45] The complete model of C IV showing each of the individual components appears in the Supplementary Materials that accompany Kaastra et al. (2014) at

individual spectra to isolate the individual emission-line fluxes and to study absorption-line variability.

4. DISCUSSION

To put the results reported here in context, we note that NGC 5548 has been monitored in the UV for RM purposes on two previous occasions, as noted in Section 1.2. In 1989, NGC 5548 was observed once every four days for eight months with *IUE* (Clavel et al. 1991). In early 1993, it was observed every other day with *IUE* for a period of two months, and during the latter part of that campaign, it was also observed daily for 39 days with the *HST* Faint Object Spectrograph (Korista et al. 1995). The primary goals of these two experiments were quite different: the 1989 campaign was the first massive coordinated RM experiment and it was designed to measure the mean lags for the strong UV lines. The 1993 campaign was a higher time-resolution experiment that was designed to eliminate ambiguities from the 1989 campaign. Specifically, its goals were:

1. To measure the lag of the most rapidly responding line, He II λ1640.

2. To determine whether or not there is a lag between the UV and optical continuum variations.

3. To determine whether the wings and core of the C IV emission line have different lags.

The first of these goals was met, but in the case of the other two, the data only hinted at results that are being confirmed by this project (Paper II and Figure 5).

In addition to these RM programs, several *HST* COS spectra of NGC 5548 were obtained in 2013 with the primary goal of studying absorption features in the UV as support for an intensive X-ray monitoring program undertaken with *XMM-Newton* (Kaastra et al. 2014). Our own results on variable absorption features constitute an extension of that effort and will be the subject of a future paper.

Again, for broader context, during the AGN STORM campaign NGC 5548 was at about the same mean continuum luminosity as it was during the 1989 campaign (but with a somewhat lower amplitude of variability), somewhat brighter than in the 1993 campaign, and decidedly brighter than it was in 2013, which was near the end of a lower-than-normal state that lasted several years (Peterson et al. 2013). The resonance lines showed much more self-absorption in this campaign than in either the 1989 or 1993 observations, but less than seen in 2013. The emission-line lags were somewhat larger during the 1989 campaign and the emission-line fluxes were higher, at least in part on account of much lower absorption in 1989. The 1993 emission-line lags were similar to those obtained in this experiment, but again the line fluxes were larger, but less self-absorbed.

As already noted, the response of the emission lines becomes complicated during the second half of the present campaign. The He II λ1640 light curve seems to match the 1367 Å continuum most closely; this line responds primarily to continuum emission at $\lambda < 228$ Å, implying that the variations in the 1367 Å continuum provide

a reasonable proxy for the behavior of the hydrogen-ionizing continuum ($\lambda < 912$ Å). He II arises closer to the central source than the other emission lines, and it is also the only non-resonance line. More detailed analysis will be undertaken once the He II λ4686 and Balmer-line results become available from our contemporaneous ground-based monitoring program (Pei et al. 2015).

In addition to determining the geometry and kinematics of the BLR, we also wish to use these data to improve on previous estimates of the mass of the central black hole. However, the strong absorption in the blue wings of the resonance lines, which was very weak if even present in the 1989 and 1993 campaigns, precludes using simple measurements of the RMS spectra (e.g., Peterson et al. 2004) to make a mass estimate. More detailed modeling that we hope will lead to a more accurate black hole mass will be undertaken in future papers.

To summarize briefly, we have presented the first results from a UV spectroscopic RM study of NGC 5548 undertaken with *HST* COS in 2014. We detect strong variations in the continuum and find clear delayed response of the strong emission lines, Lyα, N V, Si IV, C IV, and He II. A preliminary investigation shows that there is indeed a strong velocity-dependence of the emission-line lags, at least in the case of Lyα and C IV, although blending and strong resonance absorption will make interpretation challenging. However, we have also shown that a heuristic multicomponent model can account for virtually all the spectral features. In future contributions, we will use this model as a starting point to explore the UV spectral variations in detail. We will also undertake a similar analysis of contemporaneous optical spectra in an effort to more completely understand the BLR geometry and kinematics. In the accompanying Paper II, we combine the continuum light curve presented here with high-cadence observations with *Swift* for a similar reverberation study of the accretion disk structure in NGC 5548.

REFERENCES

Baldwin, J.A., et al. 1995, ApJ, 455, L119
Barth, A.J., et al. 2015, ApJS, 217, 26
Bentz, M.C., & Katz, S. 2015, PASP, 127, 67
Bentz, M.C., Peterson, B.M., Netzer, H., Pogge, R.W., & Vestergaard, M. 2009, ApJ, 697, 160
Bentz, M.C., et al. 2006, ApJ, 644, 133
—. 2007, ApJ, 662, 205
—. 2010a, ApJ, 716, 993
—. 2010b, ApJ, 720, 46
—. 2013, ApJ, 767:149
Blandford, R. D., & McKee, C. F. 1982, ApJ, 255, 419
Bottorff, M., Korista, K.T., Shlosman, I., & Blandford, R.D. 1997, ApJ, 479, 200
Brewer, B.J. , Treu, T., Pancoast, A., Barth, A.J., Bennert, V.N., Bentz, M.C., Filippenko, A.V., Greene, J.E., Malkan, M.A., Woo, J.-H. 2011, ApJ, 733, L33
Cackett, E.M., & Horne, K. 2006, MNRAS, 365, 1180
Cackett, E.M., Horne, K., & Winkler, H. 2007, MNRAS, 380, 669
Capriotti, E.R., Foltz, C.B., & Byard, P.L. 1980, ApJ, 241, 903
Cardelli, J. A., Clayton, G. C., & Mathis, J. S. 1989, ApJ, 345, 245
Clavel, J., Wamsteker, W., & Glass, I.S. 1989, ApJ, 337, 236
Clavel, J., et al. 1990, MNRAS, 246, 668
—. 1991, ApJ, 366, 64
Collier, S. J., et al. 1998, ApJ, 500, 162
—. 2001, ApJ, 561, 146
Crenshaw, D.M., & Kraemer, S.B. 1999, ApJ, 521, 572
Crenshaw, D.M., et al. 1996, ApJ, 470, 322
—. 2009, ApJ, 698, 281
De Rosa, G., Venemans, B. P., Decarli, R., Gennaro, M., Simcoe, R. A., Dietrich, M., Peterson, B. M., Walter, F., Frank, S., McMahon, R. G., Hewett, P. C., Mortlock, D. J., & Simpson, C. 2014, ApJ, 790:145
Denney, K.D., et al. 2009, ApJ, 704, L80
—. 2010, ApJ, 721, 715
—. 2014, ApJ, 796:134
Done, C., & Krolik, J,H. 1996, ApJ, 463, 144
Edelson, R., et al., submitted to ApJ (Paper II)
Elvis, M. 2004, ASP Conf. Series, Vol. 311, p. 109
Ely, J., Massa, D., Ake, T., Beland, S., Penton, S., Oliveira, C., Proffitt, C., Sahnow, D. 2011, COS FUV Gridwire Flat Field Template, Instrument Science Report COS 2011-03 (Baltimore: STScI)
Eracleous, M., & Halpern, J.P. 1994, ApJS, 90, 1
—. 2003, ApJ, 599, 886
Everett, J.E. 2003, ASP Conf. Series, Vol. 290, p. 199
Gehrels, N. 1986, ApJ, 303, 336
Gehrels, N., et al. 2004, ApJ, 611, 1005
Gezari, S., Halpern, J.P., & Eracleous, M. 2007, ApJS, 169, 167
Green, J.C., et al. 2012, ApJ, 744:60

Greene, J.E., & Ho, L.C. 2005, ApJ, 630, 122
Grier, C.J., et al. 2013, ApJ, 764:47
Grupe, D. & Mathur, S. 2004, ApJ, 606, L41
Guerras, E., Mediavilla, E., Jimenez-Vicente, J., Kochanek, C. S., Muñoz, J. A., Falco, E., & Motta, V. 2013, ApJ, 764:160
Hamann, F., & Sabra, B. 2004, ASP Conf. Series Vol. 311, p. 203
Hernandez, S., et al. 2014, STIS Instrument Handbook, Version 13.0 (Baltimore: STScI)
Holland, S.T., et al. 2014, Cosmic Origins Instrument Handbook, Version 6.0 (Baltimore: STScI)
Horne, K. 1994, in Astronomical Society of the Pacific Conference Series, Vol. 69, Reverberation Mapping of the Broad-Line Region in Active Galactic Nuclei, ed. P. M. Gondhalekar, K. Horne, & B. M. Peterson, pp. 23–51
Horne, K., Peterson, B.M., Collier, S.J., & Netzer, H., 2004, PASP, 116, 465
Horne, K., Welsh, W.F., & Peterson, B.M. 1991, ApJ, 367, L5
Jarvis, M.J., & McLure, R.J. 2006, MNRAS, 369, 182
Kaastra, J., et al. 2014, Science, 345, 64
Kaspi, S., Brandt, W.N., Maoz, D., Netzer, H., Schneider, D.P., & Shemmer, O. 2007, ApJ, 659, 997
Kaspi, S., Maoz, D., Netzer, H., Peterson, B.M., Vestergaard, M., & Jannuzi, B.T., 2005, ApJ, 629, 61
Kaspi, S., & Netzer, H. 1999, ApJ, 524, 71
Kaspi, S., Smith. P.S., Netzer, H., Maoz, D., Jannuzi, B.T, & Giveon, U. 2000, ApJ, 533, 631
Kelly, B. C., Bechtold, J., & Siemiginowska, A. 2009, ApJ, 698, 895
Kollatschny, W. 2003, A&A, 407, 461
Kollmeier, J., et al. 2006, ApJ, 648, 128
Komatsu, E., et al. 2011, ApJS, 192, 18
Korista, K.T., et al. 1995, ApJS, 97, 285
Korista, K.T., & Goad, M.R. 2000, ApJ, 586, 234
Kozłowski, S., et al. 2010, ApJ, 708, 927
Kriss, G.A., et al. 2011, A&A, 534, 41
Krolik, J.H., et al. 1991, ApJ, 371, 541
Krongold, Y., Nicastro, F., Brickhouse, N.S., Elvis, M. & Mathur, S. 2005, ApJ, 622, 842
Krongold, Y., Nicastro, F., Elvis, M., Brickhouse, N.S., Binette, L., Mathur, S., & Jiménez-Bailó, E. 2007, ApJ, 659,1022
Lewis, K.T., Eracleous, M., & Storchi-Bergmann, T. 2010, ApJS, 187, 416
Massa, D., Ely, J., Osten, R., Penton, S., Aloisi, A., Bostroem, A., Roman-Duval, J., & Proffitt, C. 2014, Updated Absolute Flux Calibration of the COS FUV Modes, Instrument Science Report COS 2013-09 (Baltimore: STScI)
MacLeod, C. L., et al. 2010, ApJ, 721, 1014
—. 2012, ApJ, 753, 106
Marconi, A., Axon, D.J., Maiolino, R., Nagao, T., Pastorini, G., Pietrini, P., Robinson, A., & Torricelli, G. 2008, ApJ, 678, 693
Mathur, S., & Grupe, D. 2005, A&A, 432, 463
McLure, R.J., & Jarvis, M.J. 2002, MNRAS, 337, 109
McGill, K.L., et al. 2008, ApJ, 673, 703
McHardy, I.M., Cameron, D.T., Dwelly, T., Connolly, S., Lira, P., Emmanoulopoulos, D., Gelbord, J., Breedt, E., Arévalo., P. & Uttley, P. 2014, MNRAS, 444, 1469
Murray, N., & Chiang, J. 1997, ApJ, 474, 91
Netzer, H., & Marziani, P. 2010, ApJ, 724, 318
Netzer, H., & Trakhtenbrot, B. 2014, MNRAS, 438, 672
O'Brien, P.T., et al. 1998, ApJ, 509, 163
Pancoast, A., Brewer, B.J., Treu, T., Park, D., Barth, A.J., Bentz, M.C., & Woo, J.-H. 2014, MNRAS, 445, 3073
Pancoast, A., et al. 2012, ApJ, 754:49
Park, D., Kelly, B. C., Woo, J.-H., & Treu, T. 2012a, ApJS, 203, 6
Park, D., Woo, J.-H., Bennert, V. N., Treu, T., Auger, M. W., & Malkan, M. A., 2015, ApJ, 799:164
Park, D., Woo, J.-H., Denney, K.D., & Shin, J., 2013, ApJ, 770:87
Park, D., Woo, J.-H., Treu, T., et al. 2012, ApJ, 747:30
Pei, L., et al. 2015, in preparation
Peterson, B.M. 1993, PASP, 105, 247
—. 2014, Space Sci. Rev., 183, 253
Peterson, B.M., & Wandel, A. 1999, ApJ, 521, L95
— . 2000, ApJ, 540, L13
Peterson, B.M., Wanders, I., Horne, K., Collier, S., Alexander. T., Kaspi, S., & Maoz, D. 1998, PASP, 110, 660
Peterson, B.M., et al. 2002, ApJ, 581, 197
—. 2004, ApJ, 613, 682

—. 2005, ApJ, 641, 638

—. 2013, ApJ, 779:109

—. 2014, ApJ, 795:149

Proga, D., et al. 2000, ApJ, 543, 686

Reichert, G.A., et al. 1994, ApJ, 425, 582

Rodríguez-Pascual, P.M., et al. 1997, ApJS, 110, 9

Salviander, S., Shields, G.A., Gebhardt, K., & Bonning, E.W. 2007, ApJ, 662, 128

Sahnow, D, et al. 2011, SPIE, 8145, 0

Schlafly, E.F., & Finkbeiner, D.P 2011, ApJ, 737:103

Schlegel, D. J., Finkbeiner, D. P., & Davis, M. 1998, ApJ, 500, 525

Scott, A.E., Brandt, W.N., Behar, E., Crenshaw, D.M., Gabel, J.R., Gibson, R.R., Kaspi, S., Kraemer, S.B., & Turner, T.J. 2014, ApJ, 797:105

Sergeev, S.G., Doroshenko, V.T., Golubinskiy, Yu. V., Merkulova, N.I., & Sergeeva, E.A. 2005, ApJ, 622, 129

Sergeev, S.G., Doroshenko, V.T., Dzyuba, S.A., Peterson, B.M., Pogge, R.W., & Pronik, V.I. 2007, ApJ, 668, 708

Shappee, B. J., et al. 2014, ApJ, 788:48

Shen, Y., Richards, G. T., Strauss, M. A., Hall, P. B., Schneider, D. P., Snedden, S., Bizyaev, D., Brewington, H., Malanushenko, V., Malanushenko, E., Oravetz, D., Pan, K., & Simmons, A. 2011, ApJS, 194, 45

Shields, G.A., et al. 2003, ApJ, 583, 124

Smith, J.D., et al. 2004, MNRAS, 350, 140

Strateva, I.V., et al. (2003), AJ, 126, 1720

Treu, T., Woo, J.-H., Malkan, M.A., & Blandford, R.D. 2007, ApJ, 667, 117

Ulrich, M.-H., & Horne, K. 1996, MNRAS, 283, 748

Vestergaard, M. 2002, ApJ, 571, 733

—. 2004, ApJ, 601, 676

Vestergaard, M., Fan, X., Tremonti, C. A., Osmer, P. S., & Richards, G. T. 2008, ApJ, 674, L1

Vestergaard, M., & Osmer, P. S. 2009, ApJ, 699, 800

Vestergaard, M., & Peterson, B.M. 2006, ApJ, 641, 689

Vestergaard, M., Wilkes, B.J., & Barthel, P.D. 2000, ApJ, 302, 56

Wakker, B. P., Lockman, F. J., & Brown, J. M. 2011, ApJ, 728, 159

Wanders, I., et al. 1995, ApJ, 453, 74

—. 1997, ApJS, 113, 69

Wills, B. J., Netzer, H., & Wills, D. 1985, ApJ, 288, 94

Wills, B.J., & Browne, I.W.A. 1986, ApJ, 302, 56

Young, S., et al. 2007, Nature, 450, 74

Zu, Y., Kochanek, C.S., & Peterson, B.M. 2011, ApJ, 735, 80